Polarimetric Analysis of Backscatter From the Deepwater Horizon Oil Spill Using L-Band Synthetic Aperture Radar

Brent Minchew, Cathleen E. Jones, and Benjamin Holt

***Abstract*—We analyze the fully-polarimetric Uninhabited Aerial Vehicle Synthetic Aperture Radar (UAVSAR) data acquired on June 23, 2010, from two adjacent, overlapping flight tracks that imaged the main oil slick near the Deepwater Horizon (DWH) rig site in the Gulf of Mexico. Our results show that radar backscatter from both clean water and oil in the slick is predominantly from a single surface scatterer, consistent with the tilted Bragg scattering mechanism, across the range of incidence angles from 26° to 60°. We show that the change of backscatter over the main slick is due both to a damping of the ocean wave spectral components by the oil and an effective reduction of the dielectric constant resulting from a mixture of 65–90% oil with water in the surface layer. This shows that synthetic aperture radar can be used to measure the oil volumetric concentration in a thick slick. Using the H/A/α parameters, we show that surface scattering is dominant for oil and water whenever the data are above the noise floor and that the entropy (H) and α parameters for the DWH slick are comparable to those from the clean water. The anisotropy, A, parameter shows substantial variation across the oil slick and a significant range-dependent signal whenever the backscatter in all channels is above the instrument noise floor. For slick detection, we find the most reliable indicator to be the major eigenvalue of the coherency matrix, which is approximately equal to the total backscatter power for both oil in the slick and clean sea water.**

***Index Terms*—Oil spill, radar polarimetry, synthetic aperture radar.**

I. Introduction

THE DEEPWATER Horizon (DWH) oil spill in the Gulf of Mexico started on April 20, 2010, and is estimated to have released 7.0×10^5 m^3 of oil before the well was capped on July 15, 2010 [1]. During the spill, extensive data from satellite and aerial remote sensing platforms were obtained to track the oil as it was transported large distances from the spill site by winds and currents. NASA sponsored the deployment of the Uninhabited Aerial Vehicle Synthetic Aperture Radar (UAVSAR) L-band polarimetric SAR to the Gulf of Mexico on June 22–23, 2010, for scientific studies of the main oil slick and the extent and impact of oil on coastal marshlands [2], [3], with the expectation that the combination of UAVSAR's quad-polarization capability, fine resolution (7 m), large swath width (22 km), stable calibration, and low noise floor could provide unique information on oil slick detection and characterization.

Oil on the sea surface effectively smooths the ocean surface and reduces the radar backscatter compared to the surrounding ocean. Marine slicks are composed of two major types of hydrocarbons, mineral oil including petroleum-based material and films from biological processes. Mineral oils come from multiple sources including spills from ships and offshore drilling platforms and pipelines, natural hydrocarbon seeps, and discharge from storm-water urban run-off. Mineral oils spread into thin layers through gravity and surface tension and evaporate and weather over time [4]. Biogenic films, also called surfactants (surface active agents) or natural films, are a viscous by-product of ocean plant and animal growth and decay. Both forms of slicks have low relative dielectric constants, with real components between 2.2 and 2.3 and imaginary components less than 0.02, over the frequency range of 0.1 to 10 GHz [5], [6]. Sea water has a higher dielectric constant, with a real component greater than 60 and absolute value of the imaginary component greater than 40 in the same frequency range [7]. Slicks generally form a thin surface layer with relatively low conductivity overlying the highly conductive sea water.

The viscoelastic properties of the marine slick material effectively dampen capillary and small gravity waves through a decrease in surface tension and a reduction in wind friction that both suppresses wave growth and increases wave dissipation [4]. Thus, the smoothed slick-covered areas appear darker than the usually wind-roughened surrounding ocean in radar images. Over the ocean, SAR detects variations in surface roughness that arise from varying wind speeds, wave-wave and wave-current interactions, and the presence of surface films. In previous slick detection studies using SAR, mineral oils have been detected at wind speeds generally between 3 and 10 m/s and may be detectable at higher wind speeds (10–14 m/s) depending on the type and density of the oil [8]–[11]. During high sea states, the slicks become mixed into the upper waters and have a reduced impact on surface roughness. Under low wind conditions, the slicks may not be distinguishable from the surrounding calm ocean that also has low radar signal return. Depending on frequency, wind speeds on the order of 2–4 m/s are required to generate sufficient small-scale waves needed to increase radar backscatter above the system

Manuscript received January 25, 2011; revised September 9, 2011 and December 19, 2011; accepted January 13, 2012. Date of publication March 8, 2012; date of current version September 21, 2012.

B. Minchew is with the Seismological Laboratory, California Institute of Technology, Pasadena, CA 91125-2100 USA (e-mail: bminchew@caltech.edu).

C. E. Jones and B. Holt are with the Jet Propulsion Laboratory, California Institute of Technology, Pasadena, CA 91109 USA (e-mail: cathleen.e.jones@jpl.nasa.gov; benjamin.m.holt@jpl.nasa.gov).

Color versions of one or more of the figures in this paper are available online at http://ieeexplore.ieee.org.

Digital Object Identifier 10.1109/TGRS.2012.2185804

noise floor of most operational instruments. Using L-band radar data acquired at incidence angles similar to UAVSAR, [12] define the threshold wind speed to be between 1.6 and 2.0 m/s.

Radar has been used to study the physical basis of the interaction of waves with both mineral and biogenic slicks. The presence of oil on the surface shifts the wave spectrum toward shorter wavelengths, reducing the surface roughness. The change in surface tension can also alter longer wavelength components of the ocean wave spectrum due to gradients in the surface tension (Marangoni effect) and indirectly through nonlinear wave-wave interactions [13]–[15]. Recent studies identify a weak intensification of wavelength components longer than 20–30 cm, related to the damping of shorter waves, elasticity of the film, and local wind wave energy balance [16]. In addition to theoretical studies, many studies have examined differentiating slicks from ambiguous ocean returns (false positives) with SAR, which generally requires repeat imaging, wind information, and knowledge of the source composition (e.g., [9], [17], [18]). Other SAR studies have also sought detection algorithms that use image classification tools, neural network methods for classification, feature vectors, wavelet transforms, and Geographic Information Systems techniques [19]–[25].

The use of multiple radar frequencies and polarizations for slick detection has also been examined, including during controlled spills of minerals and artificial biogenic oils [10], [14], [15]. These studies showed that the suppression of radar backscatter from slicks 1) increases between L-band (1.2 GHz) and Ku-band (13 GHz) frequencies; 2) shows no difference between the co-polarized channels (HH and VV); and 3) decreases with increasing wind speed. Increased suppression is seen with increasing viscosity and thickness, and heavy oils are detectable at higher wind speeds than lighter oil [10]. Interestingly, natural films appear to have increased suppression of radar returns relative to mineral oils at L-band only [15], [26]. Using the same data as [15], [27] showed that the co-polarized phase difference was able to differentiate between mineral oil and biogenic slicks at C-band but not at L-band. Nunziata *et al.* [28] developed a scattering model to account for the differences in damping or contrast found in multiple frequencies for biogenic slicks. [29] identified a non-Bragg scattering mechanism using C-band radar that occurs within oil slicks, compared to the pure Bragg scattering mechanism observed for both the ocean and biogenic slicks. The non-Bragg scattering mechanism was reportedly observed within a ship-related oil spill using L-band polarimetric data from the Advanced Land Observing Satellite Phased Array L-band Synthetic Aperture Radar sensor [30].

Given the sheer volume of oil released, the DWH spill represented a situation unlike any studied previously. The slick from the spill had widely varying oil properties spread over considerable distances that changed over time, so that the oil had a wide range of thicknesses and states of weathering. Much thicker oil layers were present relative to previous *in situ* ocean spills studied with radar remote sensing. In addition to extent, thickness is a key observable that has proven to be challenging to obtain by any sensor. Data over the DWH slick from Airborne Visible/Infrared Imaging Spectrometer (AVIRIS), a fine-resolution NASA hyperspectral sensor, have shown distinct spectral signatures with varying thicknesses between 0.1 mm and 2 mm, the range limit of its sensitivity [31].

This paper describes work to detect and characterize mineral oil slicks on water by studying the difference between polarization-dependent backscatter from areas in the main slick of the DWH spill and from surrounding Gulf waters (herein referred to as "clean" water) using data collected with the UAVSAR instrument. This study focuses on the use of L-band polarimetric backscatter to determine bulk properties of oil within the DWH oil slick. We study the characteristics of the polarized backscatter using the tilted Bragg scatter model to describe the power of the radar return and the H/A/α eigenvector decomposition to analyze the scattering properties of the oil slick relative to the surrounding water. An analysis of the noise properties of the data and the UAVSAR instrument is provided, which quantifies the effect of noise on UAVSAR's capability to detect and characterize oil slicks using parameters derived from polarimetric decomposition.

II. Theoretical Analysis

A. Radar Backscatter From the Ocean Surface

The ocean surface can be modeled as a composition of tilted, slightly rough facets, each of which is a Bragg scatterer [32]. Bragg scattering is caused by surface roughness features whose heights are small relative to the wavelength of the radar and which are randomly distributed on the scattering surface. These small height perturbations generate primarily co-polarized backscatter from ocean waves of wavenumber

$$k_B = 2k_r \sin\theta_i \tag{1}$$

where k_r is the radar wavenumber and θ_i is the incidence angle [33], [32]. In the tilted Bragg model, cross-polarized returns are introduced through a tilt caused by gravity waves on the ocean surface. The tilt of each facet is determined by the long wavelength ocean waves and defined by the angles ψ, the angle between the vertical and the projection of the tilted facet's normal onto the scattering plane, and ζ, the angle between the vertical and the projection of the tilted patch's normal onto the plane perpendicular to the scattering plane (along-track plane for the case of broadside imaging geometry). The radar incidence angle relative to the tilted facet is

$$\theta_i = \cos^{-1}\left[\cos(\theta+\psi)\cos(\zeta)\right] \tag{2}$$

where θ is the incidence angle relative to the untilted horizontal plane. The backscatter cross-section for each patch is

$$\sigma^0_{HH} = 4\pi k_r^4 \cos^4\theta_i \left| \left(\frac{\sin(\theta+\psi)\cos\zeta}{\sin\theta_i}\right)^2 R_{HH}(\theta_i) + \left(\frac{\sin\zeta}{\sin\theta_i}\right)^2 R_{VV}(\theta_i)\right|^2 \times W\left(2k_r\sin(\theta+\psi), 2k_r\cos(\theta+\psi)\sin\zeta\right) \tag{3a}$$

$$\sigma^0_{VV} = 4\pi k_r^4 \cos^4\theta_i \left| \left(\frac{\sin(\theta+\psi)\cos\zeta}{\sin\theta_i}\right)^2 R_{VV}(\theta_i) + \left(\frac{\sin\zeta}{\sin\theta_i}\right)^2 R_{HH}(\theta_i)\right|^2 \times W\left(2k_r\sin(\theta+\psi), 2k_r\cos(\theta+\psi)\sin\zeta\right) \quad (3b)$$

$$\sigma^0_{HV} = 4\pi k_r^4 cos^4\theta_i \left(\frac{\sin(\theta+\psi)\sin\zeta\cos\zeta}{\sin^2\theta_i}\right)^2 \times |R_{VV}(\theta_i) - R_{HH}(\theta_i)|^2 \times W\left(2k_r\sin(\theta+\psi), 2k_r\cos(\theta+\psi)\sin\zeta\right) \quad (3c)$$

where $W(\cdot)$ is the 2-D wavenumber spectral density of the ocean surface roughness and the Bragg scattering coefficients, R_{HH} and R_{VV}, are

$$R_{HH} = \frac{\cos(\theta_i) - \sqrt{\varepsilon_r - \sin^2(\theta_i)}}{\cos(\theta_i) + \sqrt{\varepsilon_r - \sin^2(\theta_i)}} \quad (4a)$$

$$R_{VV} = \frac{(\varepsilon_r - 1)\left\{\sin^2(\theta_i) - \varepsilon_r\left[1 + \sin^2(\theta_i)\right]\right\}}{\left(\varepsilon_r\cos(\theta_i) + \sqrt{\varepsilon_r - \sin^2(\theta_i)}\right)^2}. \quad (4b)$$

In (4), ε_r is the relative dielectric constant [32], [34], [35] and the subscripts represent the transmit and receive polarizations, respectively.

In the tilted Bragg model, the ocean wave spectrum $W(\cdot)$ is independent of polarization and cancels in the ratio of radar cross sections of different polarizations. This means that the cross-section ratios are functions of only the surface slope, the incidence angle, and the dielectric constant. If the surface dielectric properties are known, the ratio of any two of the polarization-dependent cross sections in (3) can be used to determine the tilt angles ψ and ζ, which define the root mean square (RMS) slope. The long wavelength ocean waves that contribute to the surface tilt are largely unaffected by the presence of oil on the water's surface [36], so to the extent that the tilted Bragg model is a good estimate of the surface scattering for both oil and water, the angles derived from the clean water surface can be used as an estimation of the RMS slope in an adjacent slick.

Marine slicks dampen the short wavelength ocean waves through a reduction in the surface tension at the air-liquid interface. The dispersion relationship for waves of angular frequency ω and wavenumber k at the interface between air and a liquid of density ρ with surface tension τ is

$$\omega^2 = gk + \frac{\tau}{\rho}k^3 \quad (5)$$

where g is the acceleration due to gravity. Equation (5) is the general expression for gravity-capillary waves, with gravity waves defined by the limit for small wavenumber, $\omega = \sqrt{gk}$, and capillary waves defined by the limit for large wavenumber, $\omega = \sqrt{(\tau/\rho)k^3}$. Both the density and surface tension of oil are less than those of water, with oil generally being in the range $\rho_{oil}/\rho_{water} \approx 0.8 - 0.9$ and $\tau_{oil}/\tau_{water} \approx 0.35 - 0.5$[37].

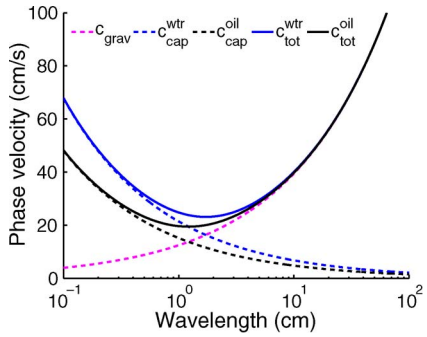

Fig. 1. Phase velocity of ocean waves as a function of wavelength in the capillary through short gravity wave part of the spectrum. The solid blue line is for clean water, and the solid black line is for oil of density 0.9 g/cm^3 and surface tension 33 dynes/cm^2. The dashed magenta line is the phase velocity of the gravity waves, which are unaffected by the change in surface tension, and the dashed blue and black lines are the phase velocity of the capillary waves for water and oil, respectively.

Ocean waves are excited by resonant forcing in a turbulent wind field [38], where equilibrium is reached when the wind speed matches the wave's phase velocity, c, where

$$c = \frac{\omega}{k} = \sqrt{\frac{g}{k} + \frac{\tau}{\rho}k} \quad (6)$$

A rigorous theoretical analysis of wind wave growth in the presence of a surface film is given by [39]. Further consideration of (5) and (6) sheds light on the general damping mechanism. Fig. 1 shows the phase velocity as a function of wavelength for water and for oil, assuming $\rho_{oil}/\rho_{water} = 0.9$, $\tau_{oil} = 33$ dynes/cm^2, and $\tau_{water} = 73$ dynes/cm^2. The graph shows the separate components of (6) in the limit $\tau = 0$ (gravity waves) and $g = 0$ (capillary waves). The lower surface tension at the air-oil interface reduces the minimum phase velocity and decreases the wavelength of the minimum energy excited waves, with an overall shift to smaller wavelengths for a given wind field as indicated in (6) and Fig. 1. The wind field varies as a function of height above the ocean surface subject to the boundary condition that the wind velocity at the ocean surface matches the water surface velocity. For wind wave generation, the ocean wave phase velocity must match the wind velocity at a height above the surface equal to one half the wavelength of the growing wind wave [12]. A given wind field over an oil layer excites shorter wavelength ocean waves in the capillary and gravity-capillary portion of the wave spectrum than over clean water. The change in surface tension affects the short gravity wave components of the ocean wave spectrum through secondary interactions, namely tangential stress in the surface tension gradients (Marangoni effect) and wave-wave interactions that shift energy between different wavenumber components of the spectrum [13]–[15], [39], [40]

The damping ratio for microwave backscatter of a given polarization JK

$$\left(\frac{\sigma_{water}}{\sigma_{oil}}\right)_{JK} = \mathcal{F}_{JK}(R)\left(\frac{W_{water}(k_B)}{W_{oil}(k_B)}\right) \quad (7)$$

is a function of the Bragg coefficients, R_{HH} and R_{VV}, (denoted here by $\mathcal{F}(\mathcal{R})$) and the ratio of the wave spectra at the Bragg wavenumber in clean water to that in the slick.

At L-band, where the Bragg wavenumber is in the short gravity wave region, the wave spectrum for the slick is only affected through secondary interactions, not through a direct effect of the reduced surface tension. For a thin oil film on top of water, where the radiation penetrates to the underlying sea water surface from which it scatters, $\mathcal{F}$ is approximately unity because the scattering occurs mainly from the water interface and is governed by the dielectric properties of the water. However, the volume of the DWH spill was extensive, and the oil traveled from depth 1.7 km to reach the surface, during which the oil plume entrained sea water [41]. For the DWH slick, the upper layer of the ocean surface was likely a mixture of water and oil, and in this case, the damping ratios are functions of the dielectric properties of both water and oil. In this paper, we show that the oil in the DWH slick was likely mixed with sea water in the upper layer with thickness on the order of the skin depth, which is 7–9 mm for sea water [7].

B. Polarimetric Decomposition

Averaged Coherency Matrix: The relationship between the incident and scattered electric fields in a monostatic radar system is

$$\begin{bmatrix} E_H \\ E_V \end{bmatrix}_{scat} = \begin{bmatrix} S_{HH} & S_{HV} \\ S_{HV} & S_{VV} \end{bmatrix} \begin{bmatrix} E_H \\ E_V \end{bmatrix}_{inc} \tag{8}$$

where the elements of the 2×2 matrix (which is sometimes referred to as the Sinclair, Jones, or scattering matrix) are complex and fully define the scattering in the far field. In order to relate the polarimetric backscatter to the physical properties of the scatterer, we form the target vector $\mathbf{k}$ in the 3-D Pauli basis [42]–[45]

$$\mathbf{k} = \frac{1}{\sqrt{2}}[S_{HH} + S_{VV} \quad S_{HH} - S_{VV} \quad 2S_{HV}]^T. \tag{9}$$

The coherency matrix $\mathbf{T}_3$ is defined as the product of the target vector with its complex conjugate transpose

$$\mathbf{T}_3 = \mathbf{k}\mathbf{k}^{*T} \tag{10}$$

and the averaged coherency matrix $\langle \mathbf{T}_3 \rangle$ is defined as [43]–[45]

$$\langle \mathbf{T}_3 \rangle = \frac{1}{N} \sum_{i=1}^{N} \mathbf{T}_{3_i} \tag{11}$$

where the sum is taken over adjacent pixels in the image to reduce speckle noise and quantify scattering from distributed targets. The diagonal terms of $\mathbf{T}_3$ are the backscattered power of each of the Pauli scattering elements, and the off-diagonal terms of $\mathbf{T}_3$ are the complex correlation components between the Pauli elements. The total backscatter power, σ_T, is derived from scattering matrix $\mathbf{S}$ (8) or $\mathbf{T}$ as

$$\sigma_T = Span(\mathbf{S}) = Trace(\mathbf{T}_3). \tag{12}$$

The coherency matrix $\mathbf{T}_3$ is a positive semidefinite Hermitian matrix and can be diagonalized as [44]

$$\langle \mathbf{T}_3 \rangle = [\mathbf{U}_3][\mathbf{\Omega}][\mathbf{U}_3]^{-1} \tag{13}$$

where $\mathbf{\Omega}$ is a 3×3 diagonal matrix that contains the nonnegative real eigenvalues $(\lambda_1 \geq \lambda_2 \geq \lambda_3)$ and $\mathbf{U}_3$ is the 3×3 unitary matrix whose columns are the mutually orthogonal eigenvectors expressed in the 3-D Pauli basis. The eigenvectors can be written as

$$\mathbf{u}_i = \begin{bmatrix} \cos\alpha_i e^{j\phi_i} \\ \sin\alpha_i \cos\beta_i e^{j(\delta_i+\phi_i)} \\ \sin\alpha_i \sin\beta_i e^{j(\gamma_i+\phi_i)} \end{bmatrix} \tag{14}$$

where α_i is the scattering parameter that represents an internal degree of freedom of the scatterer and is independent of the physical orientation of the radar with respect to the scatterer [46]. β_i is the orientation of the scatterer about the radar line of sight, and ϕ_i, δ_i, and γ_i are phase shifts between the different polarization-dependent components. Because the coherency matrix is Hermitian, its eigenvalues are constant under unitary transformations. The result is that all of the decomposition elements calculated from the eigenvalues are roll invariant about the radar line of sight [43]. It can be shown that of the eigenvector parameters, only the angle α is roll invariant [43], [44].

H/A/$\bar{\alpha}$ Eigenvector Decomposition Elements: Some previous studies of oil slicks [e.g., [47], [48]] have investigated the potential of evaluating the stochastic properties of the slick scattering surface using the well-known H/A/$\bar{\alpha}$ polarimetric decomposition method [44]. This method utilizes complementary elements calculated from the eigenvalues and eigenvectors of the averaged coherency matrix $\langle \mathbf{T}_3 \rangle$. Spatial averaging enables analysis of the properties of spatially distributed scatterers rather than single point scatterers. The decomposed elements of the averaged coherency matrix show whether there exists a dominant scatterer and defines the scattering mechanism of the most dominant scatterer(s) [44].

The H/A/$\bar{\alpha}$ eigenvector decomposition utilizes three values calculated from either the eigenvalues or eigenvectors of the coherency matrix called the entropy (H), anisotropy (A), and the averaged scattering parameter $(\bar{\alpha})$[44]. Each of these elements provide different, but not unique, information about the scatterer.

Entropy is the measure of randomness in the distributed scatterer and is defined from the logarithmic sum of the eigenvalues as

$$H = -\sum_{i=1}^{3} p_i log_3(p_i) \quad 0 \leq H \leq 1 \tag{15}$$

where

$$p_i = \frac{\lambda_i}{\lambda_1 + \lambda_2 + \lambda_3} = \frac{\lambda_i}{\sigma_T} \quad 0 \leq p_i \leq 1. \tag{16}$$

Low entropy $(H <\approx 0.3)$ is indicative of a deterministic single dominant scatterer, while high entropy $(H >\approx 0.7)$ indicates random scattering [44].

Anisotropy measures the relative values of the second and third eigenvalues [44] and is defined as

$$A = \frac{\lambda_2 - \lambda_3}{\lambda_2 + \lambda_3} \quad 0 \leq A \leq 1. \tag{17}$$

When anisotropy is zero, the scattering mechanism is azimuthally symmetric. Therefore, anisotropy can also be considered the measure of the lack of azimuthal symmetry or as an indication of small-scale surface roughness [47], [49]. Whenever entropy is low ($\lambda_1 \gg \lambda_2$) anisotropy is highly affected by noise [45]. We expect UAVSAR to provide better evaluations of anisotropy in low entropy areas because UAVSAR has a higher signal-to-noise ratio (SNR) (discussed later) than any other operational SAR system.

The mean scattering parameter, $\bar{\alpha}$, which is calculated from the eigenvectors, $\mathbf{u}_i$, of (14) as

$$\bar{\alpha} = \sum_{i=1}^{3} p_i \alpha_i \quad 0^\circ \leq \alpha \leq 90^\circ \tag{18}$$

indicates the types of scattering mechanisms present in the distributed target. Over the ocean, we can expect a dominant surface scattering component, so $\bar{\alpha}$ for the free ocean surface in moderate winds is less than 42.5° and increases with increasing incidence angle. When volume scattering becomes a primary contributor to the total backscatter, $\bar{\alpha}$ is greater than 42.5°. When ships are present, $\bar{\alpha}$ should be greater than 60°[44].

For Bragg scattering from an untilted, horizontal surface, the coherency matrix has a single dominant eigenvalue ($\lambda_1 > 0, \lambda_2 \approx 0, \lambda_3 \approx 0$) whose corresponding eigenvector is

$$\begin{aligned} \mathbf{u}_1 &= \mathbf{k}_{Bragg} \\ &= \frac{1}{\sqrt{2}}[S_{HH} + S_{VV} \quad S_{HH} - S_{VV} \quad 0]^T \\ &\approx m_s[R_{HH} + R_{VV} \quad R_{HH} - R_{VV} \quad 0]^T \end{aligned} \tag{19}$$

where m_s is the roughness coefficient [49]. In this case, the entropy is very low. The scattering parameter, $\bar{\alpha} \approx \alpha_1$, is independent of surface roughness and increases as a function of only the dielectric constant and incidence angle [45], [50] as

$$\tan(\alpha) \approx \frac{|R_{HH} - R_{VV}|}{|R_{HH} + R_{VV}|}. \tag{20}$$

III. *In Situ* Oil Spill and Environmental Observations

The oil released from the DWH well is classified as Mississippi Canyon Block 252 (MS252) (South Louisiana sweet crude) oil, which is a comparatively light crude that contains significant quantities of natural gas when released. The characteristics of the surface oil in the main slick varied greatly, from thicker layers of crude to thinner sheens, and a range of aggregated and weathered forms of oil-water emulsion. On June 23, 2010, the second day of the UAVSAR campaign and the day that the main spill site was imaged, the containment cap, which had been successfully capturing significant quantities of oil for removal to ships, had to be removed because of a mishap when a robotic arm hit one of the vents in the cap. The removal of the cap thus restarted the release of the full flow rate of oil so at the time of the UAVSAR overflights the oil in the study area was mainly freshly released. Fig. 2 is a photograph of the surface oil taken near the spill site on June 23, 2010.

Fig. 2. Surface oil near the Deepwater Horizon rig site on June 23, 2010. (Photograph provided by Oscar Garcia-Pineda, Florida State University).

During the period of the oil spill, there were numerous daily overflights by multiple aerial platforms to provide information and photography on extent and oil properties for first responders. These include NOAA aerial and helicopter imagery and observations (https://sftp.orr.noaa.gov/deepwater_horizon_ext/); imagery from the Environmental Protection Agency (http://www.epa.gov/bpspill/epa.html); and multiple aerial and satellite data sets at the U. S. Geological Survey archive (http://hdds.usgs.gov/hdds/tier1/index.php?disaster=201004_Oilspill_GulfOfMexico).

We identified a series of aerial images and observer information over the main body of the slick obtained within approximately 7 h of the time of acquisition of the two UAVSAR flight tracks, which occurred between 20:40 and 21:40 UTC. Fig. 3 shows representative aerial images near the primary spill site. Based on these collective observations and interpretation of the properties of the oil from the photographs, we determined that the bulk of the oil spill sampled by the UAVSAR was composed primarily of brown emulsified oil, ranging from red to brown in color, mixed with thinner (silver and rainbow) sheen layers. Dispersants are thought to have been applied to portions of the slicks [Fig. 3(c) and (d)] because of the cloudy nature of the slick appearance. The dispersants break down the slicks into particles or droplets, which then settle into the water column at least to shallow depths, thus forming a cloudy appearance rather than the streaky slicks seen in Fig. 3(b). Based on the NOAA field guide for aerial observations [51], these types of oils have the following range of thicknesses: emulsified oils $-$ 0.2 to 3 mm with a mean of 1 mm; rainbow sheen $-$ 0.0003 to 0.005 mm and mean $= 0.001$ mm; silver sheen $-$ 0.00004 to 0.0003 mm with a mean of 0.0001 mm.

Both buoy data and Wavewatch III postdictions were used to obtain the sea surface conditions at the time that the UAVSAR data were acquired. The wave model indicates that the surface conditions were nearly uniform over the area used in our analyses. At the nearby ocean buoy Station 42887 (28.191° N, 88.496° W), from 1200–1700 UTC, wind speeds ranged between 4 and 6 m/s with directions from 130° to 160°, with waves of significant wave heights of 1.0–1.5 m and

Fig. 3. Samples of aerial photography of the DWH oil spill taken on June 23, 2010. (a) EPA ASPECT overflight photograph 55–053, obtained at 16:50:27 UTC, 28.9393° N, 88.4884° W, showing brown-black emulsion within thin sheen; (b) RAT HELO overflight photograph 428, obtained at 19:53:00 UTC, 28.7288° N, 88.4170° W, showing ship wake induced brown-black emulsion lines and thin sheen; (c) RAT HELO overflight photograph 431, obtained at 19:53:31 UTC, 28.7256° N, 88.3988° W, showing the DWH site with brown emulsion and cloudy areas likely formed by applied dispersants; and (d) RAT HELO overflight photograph 453, obtained at 19:56:57, 28.7449° N, 88.3861° W, showing DWH rig site with brown emulsion and cloudy areas likely formed by applied dispersants. The same platform (P1) is identified at the DWH spill site in C and D to indicate scene overlap and orientation.

periods 4–7 s. Between 1700 and 2200 UTC, a wind shift took place toward directions 115°–126° accompanied by a slight reduction in speed to between 2.5 and 5 m/s and a lowering of significant wave heights to 1.0–1.3 m with little change in wave period. At the closest directional wave buoy Station 42012 (30.065° N, 87.555° W), the dominant wave direction from 12:00 to 22:00 UTC was from between 115°–145° True, with significant wave heights of 0.85 m decreasing to 0.57 m, with wave periods of 4.5 to 6.3 s, and an ocean temperature of 31.2 °C.

By examining coastal HF radar surface current data for June 23, 2010 (http://cordc.ucsd.edu) within the approximate area of the spill site, we determined that currents were generally northward until about 1700 UTC, when the currents shifted toward the east and south at the time of the UAVSAR flights, opposing the wind direction at those times. These variations in winds and currents likely explain the offsets seen between some of the earlier visual observations and the SAR spill coverage and features.

IV. UAVSAR Data

The UAVSAR platform is a Gulfstream-3 aircraft instrumented with a L-band polarimetric SAR that operates with 80 MHz bandwidth from 1.2175–1.2975 GHz [52]. The radar transmits and receives in both horizontal (H) and vertical (V) (quad-polarization) modes. UAVSAR images a 22-km-wide ground swath at 22°–65° incidence angles. The combination of the UAVSAR full polarization capability with an extremely low noise floor makes it an excellent instrument for polarimetric SAR studies. The noise equivalent σ_0 of the system is -53 dB at its minimum near the midrange of the swath. More information about the instrument noise is included in Appendix A. The UAVSAR radar has 1.2-dB absolute calibration and 0.5-dB relative calibration between the amplitudes of the different polarization transmit/receive channels (private communication, Scott Hensley). More information on the radar operating characteristics during the Gulf of Mexico flights is given in Table I.

TABLE I
UAVSAR Radar Operational Parameters

Frequency	1.2575 GHz
Wavelength	0.2379 m
Bandwidth	80 MHz
Pulse Duration	40 μs
Polarization	Quad Polarization
Operating Altitude	12.5 km
Ground Speed	220 m/s
Range Swath	22 km
Look Angle	22° – 65°
Slant Range Resolution	1.7 m
Azimuth Resolution	1.0 m
Transmit Power	3.1 kW
Cross Pol Isolation	-25 dB

The two flight lines used in this study are gulfco_14010_10054_100_100623 (collection time 23-June-2010 20:42 UTC and hereafter referred to as 14010), which passed directly over the DWH rig site at a heading of 140°, and gulfco_32010_10054_101_100623 (collection time 23-June-2010 21:08 UTC and hereafter referred to as 32010), which passed immediately to the west of and parallel to 14010 along a 320° heading. UAVSAR single look complex products are processed with 1.7-m slant range resolution and 1-m azimuth (along-track) resolution. For this analysis, we used multilook complex products

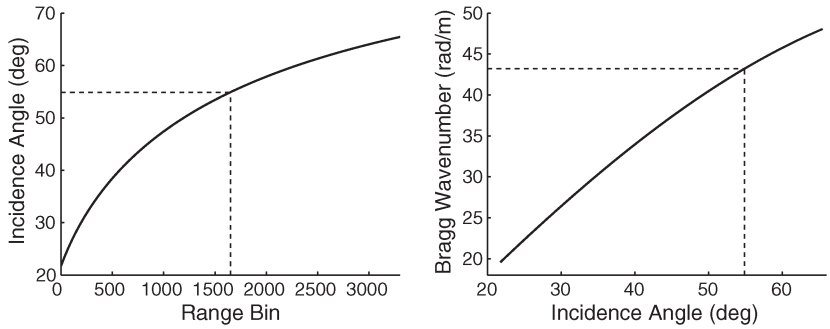

Fig. 4. (Left) Incidence angle versus range bin for the UAVSAR imaging geometry. The black dotted lines indicate the midrange incidence angle of 54.9°. (Right) Bragg wavenumber versus incidence angle.

for the HH, HV, and VV normalized radar cross section (NRCS), which have three range (cross-track) and 12 azimuth (along-track) looks and a pixel spacing of 5 m in slant range and 7.2 m in azimuth. All images shown in this paper are in slant range and azimuth coordinates. The transect plots in this paper are shown as a function of incidence angle and, in some cases, Bragg wavenumber. The incidence angle plotted is calculated for an untilted ocean surface. The relationship between range pixel number, incidence angle, and Bragg wavenumber is given in Fig. 4. For UAVSAR, the Bragg wavelength varies from 32 cm at near range to 13 cm at far range.

V. Noise Analysis

A. Noise Equivalent Sigma Zero

Radar backscatter from oil and other look-alikes, such as low wind areas and biogenic films, return only a small portion of the incident radar power, making the influence of the noise equivalent sigma zero (NESZ) of a given instrument an important consideration in data analysis. The NESZ, also called the instrument noise floor, is the radar backscatter cross section of equivalent signal level to that from the noise of the instrument and represents the limit of the detectable backscatter signal. Instrument noise included in the NESZ is Gaussian white noise whose mean and variance are approximately equal for horizontal and vertical receive polarizations. We determined the UAVSAR NESZ from receive-only data collected during line 32010 over the DWH spill, as detailed in Appendix A. To evaluate the proximity of the instrument noise floor to the data considered in this study, we compare the measured NESZ with the NRCS of backscatter for each polarization. In Section VI, the NESZ is plotted along with the NRCS for each polarization to show the proximity of the observed backscatter to the instrument noise floor. We find that at higher incidence angles, the HV return from oil, which is consistently the lowest power return, is close to the noise floor, indicating a low SNR. Following [53], we define a measured return power threshold of 6 dB above the noise floor $(\mathrm{SNR} \leq 3)$ and indicate data that are below this threshold on the appropriate plots with a gray shaded region for data over oil and a blue dotted line for data over clean water. Any data that are below this threshold are considered to be corrupted by instrument noise and unsuitable for analysis of the scattering properties. However, we retain the noisy data to demonstrate the effect of instrument noise on the analysis.

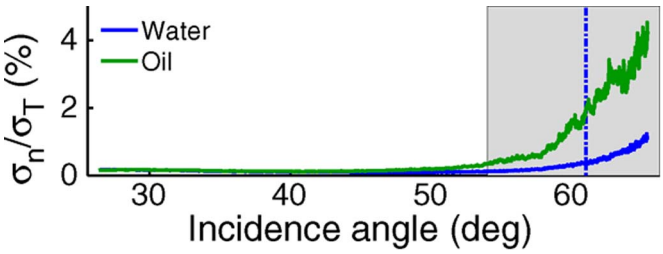

Fig. 5. Contribution of the averaged noise power σ_n, calculated using the filtering procedure of [49], to the total return power σ_T for a representative water and oil transect. The gray shaded region indicates the region of the data where HV power over oil is within 6 dB of the instrument noise floor, and the vertical blue dashed line indicates the incidence angle above which the HV power in the clean water data is within 6 dB of the instrument noise floor.

B. Noise Reduction and Quantification

Polarimetric SAR data and the associated decomposition methods are sensitive to noise and speckle, a natural phenomena caused by the coherent interference of microwaves that are reflected by numerous small-scale scatterers. To mitigate the influence of noise and speckle and to minimize multilook bias, we performed a moving average of the components of the coherency matrix over a 9×9 window prior to calculating the eigenvalues and eigenvectors [54], [55]. To evaluate whether residual noise remained, we estimated the average noise power σ_n following the filtering process outlined in [49] and detailed in Appendix B. This process is based on the principle that although the HV and VH returns in an ideal monostatic SAR system are identical, in the presence of noise, the two cross-polarized channels have slightly different returns. During standard UAVSAR product generation, the UAVSAR HV and VH returns are averaged after crosstalk calibration and distributed as HV data. Using the calibrated single-look complex (SLC) data, we evaluate the noise power by considering HV and VH as independent measurements and show that the residual noise power is less than 0.5% of the total scattered power whenever the HV (and VH) backscatter power is above the SNR threshold. At low to intermediate incidence angles, the noise power is approximately 0.1% of the total power (Fig. 5). This noise analysis also shows that below approximately 45° local incidence angle (AOI), there is little difference between the noise over oil and over water. Therefore, we consider the contribution of noise to the data to be negligible whenever the scattered power in all three polarization channels is above the SNR threshold. An analysis of the effect of removing the measured noise power

from the coherency matrix $\mathbf{T}_3$ is provided in Appendix B. We find that filtering does not change the relative values between oil and water of the eigenvalue-based parameters, but filtering does scale the absolute values of the entropy and anisotropy for both water and oil. Because this noise analysis and subsequent filtering require special processing using the UAVSAR processing software and either the quad-polarization SLC or raw UAVSAR data (none of which are publically available) and because the results are not significantly affected by the filtering procedure, the data presented hereafter use the standard calibrated UAVSAR normalized backscatter products without filtering.

It is worth noting here that high averaged noise power in data that are below the SNR threshold is indicative of the randomness of instrument noise (shaded region of Fig. 5). Because the two returns for the different polarizations are received at different times, the averaged noise power calculated using the difference between the HV and VH backscatter is always nonzero. Consequently, if the received power in one or more of the polarization channels is near the noise floor, instrument noise will induce an apparent randomness in the data that does not represent the physical properties of the scatterer. The steep slope of the NESZ at high incidence angles and the continual decline in the received power of the HV channel causes the contribution of noise to the overall signal to increase rapidly when the signal is near the instrument noise floor.

VI. UAVSAR Results

We analyze three oil-contaminated segments and one clean water segment from each of the two UAVSAR flight tracks that imaged the main slick of the spill (14010 and 32010). The range and azimuth boundaries for all of the segments are given in Table II, and the segments are outlined and labeled in the vertical co-polarized intensity images of the study area (Fig. 6). The DWH rig site location is at the bottom of the slick in Fig. 6(b), near coordinates (1800, 6400). For reference, the bold crosses in these two images show a common point in the overlap region of the two swaths. The bright points in the water near the DWH rig site are surface vessels and platforms; other surface vessels show up as isolated bright points elsewhere in the image, often with disturbed oil in their wake. Of the six segments analyzed in our study, segment Oil 6 is closest to the rig site, with segment Oil 5 only slightly further away. We note that in Fig. 6, the comparatively smooth edge on the SE side of the spill and the dispersing oil on the NW side provides an indication of the prevailing wind direction and matches well with the buoy measurements presented in Section III.

We evaluated the along-track mean for all segments listed in Table II to form transects across the slick as a function of incidence angle. We present the resulting NRCS transects for both flight tracks, but for brevity later in the analysis, we include only track 32010 results for the eigenvalue decomposition and note that the general results are the same for both flight tracks. The along-track means are plotted as a function of local incidence angle (AOI) to demonstrate the varying nature of oil in a SAR scene over the span of incidence angles commonly imaged by SAR systems. We exclude AOIs below approximately 26° because specular scattering is dominant, and as a result, little information that characterizes oil and water based on Bragg scattering is available in this data. Data at high incidence angles are also presented to illustrate the influence of system noise. When applicable, the profile plots are shaded to indicate when the data are below the noise threshold discussed in Section V-A. The shaded region indicates when the smallest NRCS of the three oil transects falls below the SNR threshold; in some cases, one or both of the other oil transects have NRCS

TABLE II
AZIMUTH LINE (AL) AND RANGE BIN (RB) BOUNDARIES FOR THE CLEAN WATER AND OIL-ON-WATER SEGMENTS IN EACH FLIGHT TRACK USED IN THE ANALYSIS. (TO CONVERT THE GIVEN AL VALUES FOR 14010 TO THE AL VALUES IN THE FULL STRIP THAT IS AVAILABLE FROM THE ALASKA SATELLITE FACILITY, ADD 23 600; THE AL VALUES FOR 32010 ARE THE SAME IN THE FULL STRIP.)

32010				
Region	First AL	Last AL	Near RB	Far RB
Water 1	100	1600	100	3280
Oil 1	2450	2650	100	3280
Oil 2	3500	3800	100	3280
Oil 3	4150	4450	100	3280
14010				
Region	First AL	Last AL	Near RB	Far RB
Water 2	1375	2425	100	3280
Oil 4	4125	4400	100	3280
Oil 5	4935	5080	100	3280
Oil 6	5125	5575	100	3280

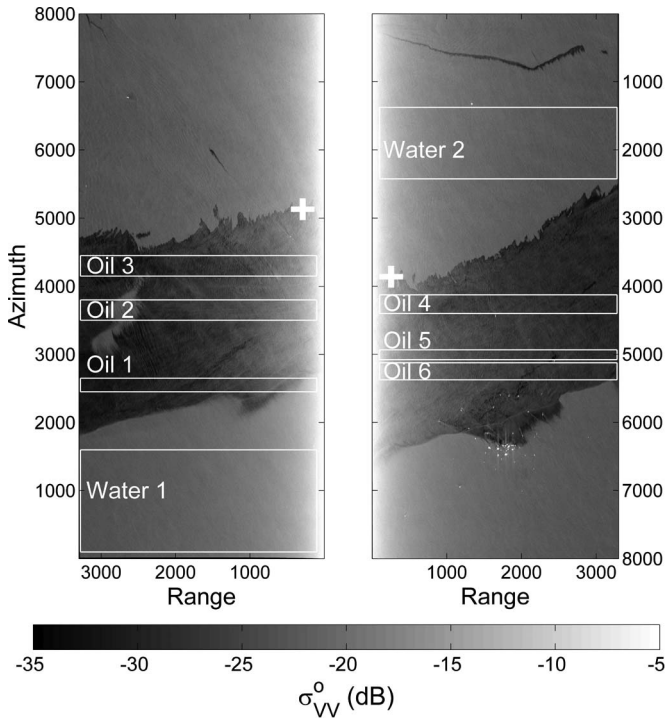

Fig. 6. Vertical co-polarized normalized radar cross section, σ_{VV}, images for 32010 (left) and 14010 (right) showing the cross-track segments that are evaluated in detail. One clean water and three oiled segments (shown in white-outlined boxes) are used for each flight line. The bold crosses in the two images show a common point in the overlap region of the two swaths. The small white spots in image 14010 around azimuth line 6500 and midrange are surface vessels and platforms at the Deepwater Horizon site. Many other white spots are also surface vessels. The range and azimuth axes are in pixel units, with pixel size 7.2 m in azimuth and 5.0 m in slant range.

above the SNR threshold at the lower incidence angles in the shaded region.

We note the following persistent features within the data segments. The high NRCS area at approximately 62° AOI in the Oil 2 segment is an area of clean water surrounded by oil which can be seen in Fig. 6(a) centered at approximately (2800, 3500) and spanning 500 range bins and 1000 azimuth bins. This feature will be present throughout the data and helps demonstrate the distinct behavior of the radar signals from oil versus clean water. The section of the Oil 1 segment below 35° AOI is also an area of water to the windward side of the slick that shows very little surface oil contamination.

A. Normalized Radar Cross Sections

In the NRCS data, we observe reduced backscatter from oil in the slick relative to clean water across all incidence angles and for all polarizations (Fig. 7). The inset graph at the upper right in each frame shows the instrument noise floor (NESZ) plotted on the same scale as the measured cross sections to emphasize that the measured values are significantly above the instrument noise at all but the highest incidence angles. On the plots of the HH and HV NRCS, the gray regions show where the NRCS over one or more of the oil transects are within 6 dB of the noise floor; and the vertical blue line shows the incidence angle where the NRCS over water falls to within 6 dB of the noise floor. The VV NRCS for both oil and water exceeds the noise floor by more than 6 dB at all accessible incidence angles.

The co-polarized ratio, $\sigma^0_{HH}/\sigma^0_{VV}$, readily distinguishes oil from water and, in the tilted Bragg model, is independent of the ocean wave spectrum, i.e., of the damping of the gravity-capillary waves by oil (Fig. 8). This means that the co-polarized ratio is a function of only the dielectric constant, RMS slope due to long wavelength ocean waves, and incidence angle. Because the long wavelength ocean waves that govern the RMS slope are largely unaffected by the presence of oil or other surface contaminates, the difference in the co-polarized ratio for oil and water shows that the reduction in backscatter over oil in the DWH slick is at least partially due to differences in the dielectric constant.

Before we could estimate the effective dielectric constant for the mixture of oil and water from the oil NRCS ratios, we estimated the tilt of the Bragg scattering planes as follows. Assuming a dielectric constant for sea water of $80 - i70$, we estimate the slope angles ψ and ζ by fitting the clean water σ_{HH}/σ_{VV} curve using numerical optimization. We find that varying the value of the imaginary component of the sea water dielectric constant within its range of values for sea surface temperatures between 0° and 40° has little effect on the value of the theoretical co-polarized ratio and, therefore, the value of the estimated slopes. The RMS slope, calculated as the RMS of ψ and ζ, is 6.4° for flight track 32010 and 7.2° for flight track 14010. The clean water data in each flight track were acquired near the slick during the same data acquisition so the estimated slope angles are valid for both clean water and oil.

After estimating the slope angles, we estimate the upper and lower bounds of the dielectric constant for oil (dielectric constant of crude oil is assumed to be $2.3 - i0.02$ [5], [6]) by adjusting the volumetric concentration of oil in a mixture of oil and sea water. The estimated limits for the oil volumetric concentration are 75% and 90% for track 32010 and 65% and 85% for track 14010. Hereafter, we use an effective dielectric constant for a mixture of 80% oil and 20% sea water for calculations of theoretical values for oil. The difference in the apparent oil concentration between the two flight lines could indicate less complete mixing in the oil that is close to the DWH site.

We invert the NRCS values for the ocean spectral density at the Bragg wavenumber, $W(k_B)$, using the estimated slope angles and dielectric constants (Fig. 9). We use the VV NRCS for the inversion because the values are above the SNR threshold at all incidence angles for both oil and water. The calculated W values are smaller for the oil lines than for the water lines as expected. We then fit the W values for water and for all of the oil data in each line. After calculating W from the VV NRCS, we calculate the theoretical NRCS values from the tilted Bragg model for all polarizations and compare them to the data (Fig. 7). All of the NRCS data show good agreement with the tilted Bragg model using our fit values for the RMS slopes and wave spectral densities. For comparison, theoretical values are calculated to simulate a low-wind area by using the dielectric constant of sea water and the W calculated from the oil data in the tilted Bragg model (light blue dotted line in Fig. 7).

B. Damping Ratios

The water-to-oil NRCS ratios, or damping ratios [(7)], give information about the ocean spectral density at the Bragg wavelength and, for thick slicks, the dielectric properties of the surface layer. The damping ratios for the clean water and oil transects in lines 32010 and 14010 are shown in Fig. 10 for HH, VV, and HV returns, with the region where the minimum oil return falls below the SNR threshold indicated in gray. In general, the damping ratios for all oil transects show a systematic increase with increasing Bragg wavenumber for return power above the SNR threshold, though the HV and HH values suggest that at higher Bragg wavenumber, this trend might change. However, the influence of instrument noise in each channel precludes the possibility of observing higher Bragg wavenumbers. The results are consistent with the theoretical tilted Bragg model discussed in Section II-A, although the nonuniformity of the oil in the slick affects the damping ratio significantly. In general, the damping ratio is smaller for the lines closest to the rig site (Oil 5 and Oil 6).

Fig. 10 also show the damping ratio of the ocean wave spectral density, W_{water}/W_{oil}, derived from the VV NCRS. Where the data are above the SNR threshold, we find that the wave spectral damping increases with increasing wavenumber as expected from the dispersion relationship. The differences between the measured damping ratios and the value of W_{water}/W_{oil} derived from the fit come mainly from the change in the surface dielectric constant in the slick. Variations in the damping ratio between the different oil transects are attributable to variation in the oil concentration, thickness, or dielectric properties and to variations in the ocean wave spectral density not captured by the average fit to either W_{water} or W_{oil}. The

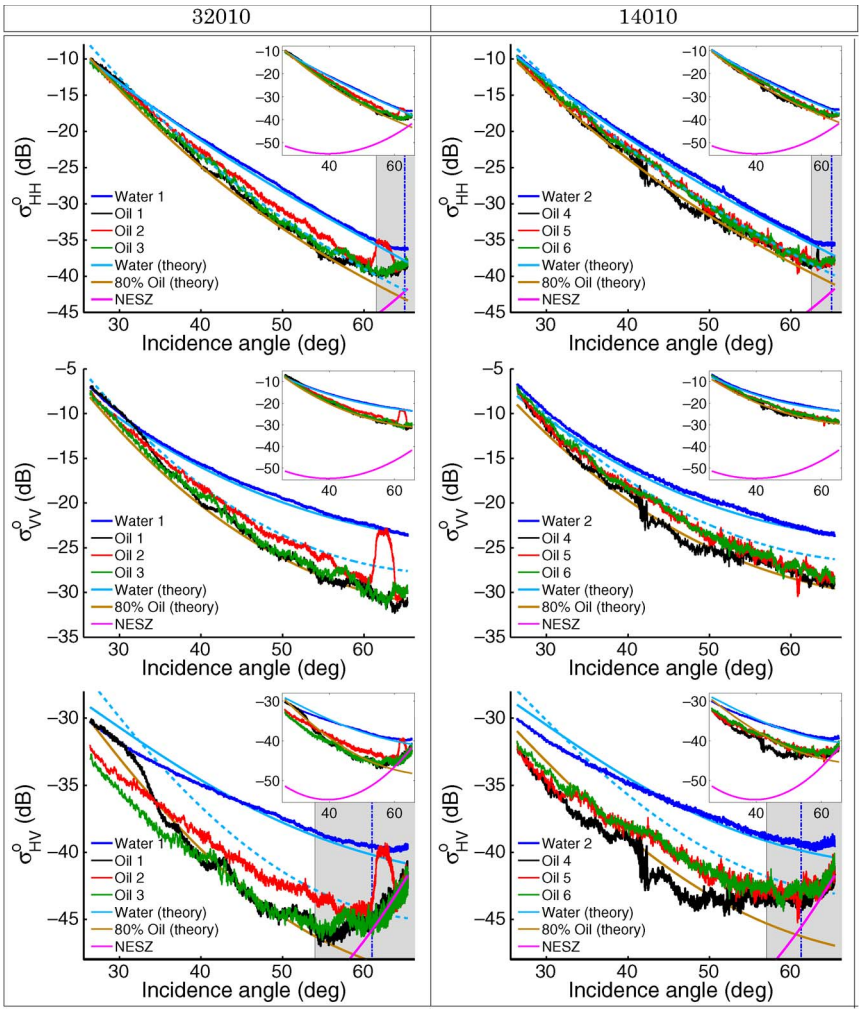

Fig. 7. Polarized NRCS derived from multilooked UAVSAR data. The imbedded images are zoomed-out versions of the respective NRCS to show the NESZ. Theoretical values are shown in solid light blue for water and solid brown for a mixture of 80% oil and an RMS slope of 6.4° for flight track 32010 (left column) and 7.2° for 14010 (right column). The dotted light blue line shows the theoretical values for a surface with sea water dielectric constant and the ocean wave spectral density of oil to simulate the expected radar returns from a low-wind area of clean water.

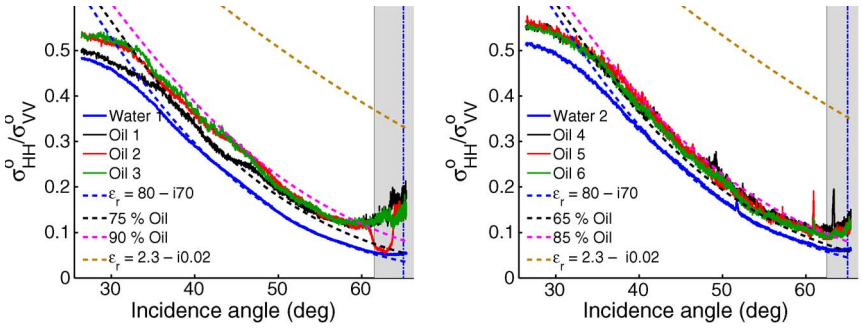

Fig. 8. Co-polarized NRCS ratio for HH/VV and theoretical values calculated from the tilted Bragg model for sea water ($\varepsilon_r = 80 - i70$) and different volumetric concentrations of oil for track 32010 (left) and 14010 (right), including oil only. The oil-only line (brown dotted line) is far from the oil/water mixture lines because the dielectric constant for sea water is much larger than for oil. For the theory, the RMS slopes were derived from the clean water co-polarized NRCS ratio.

damping ratios are similar to those discussed for L-band and mineral oil by [15].

We note that the damping ratios are slightly different between the data from the two flight lines, which observed the spill from opposite look directions. Most of this difference is accounted for by the different RMS slopes for the two directions. This difference is probably due to the influence of wind direction on the wave peaks, which generates an upwind-downwind asymmetry between the wave amplitude profiles and the radar backscatter. Also, the damping ratios appear to increase away from the rig site, perhaps due to increased mixing over distance related to the incoming wind and wave fields from the east-southeast. The

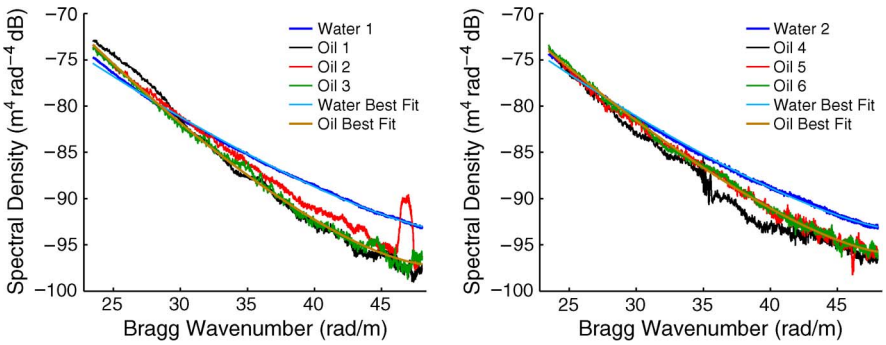

Fig. 9. Spectral density of the ocean surface roughness $W(k_{Bragg})$ for track 32010 (left) and 14010 (right).

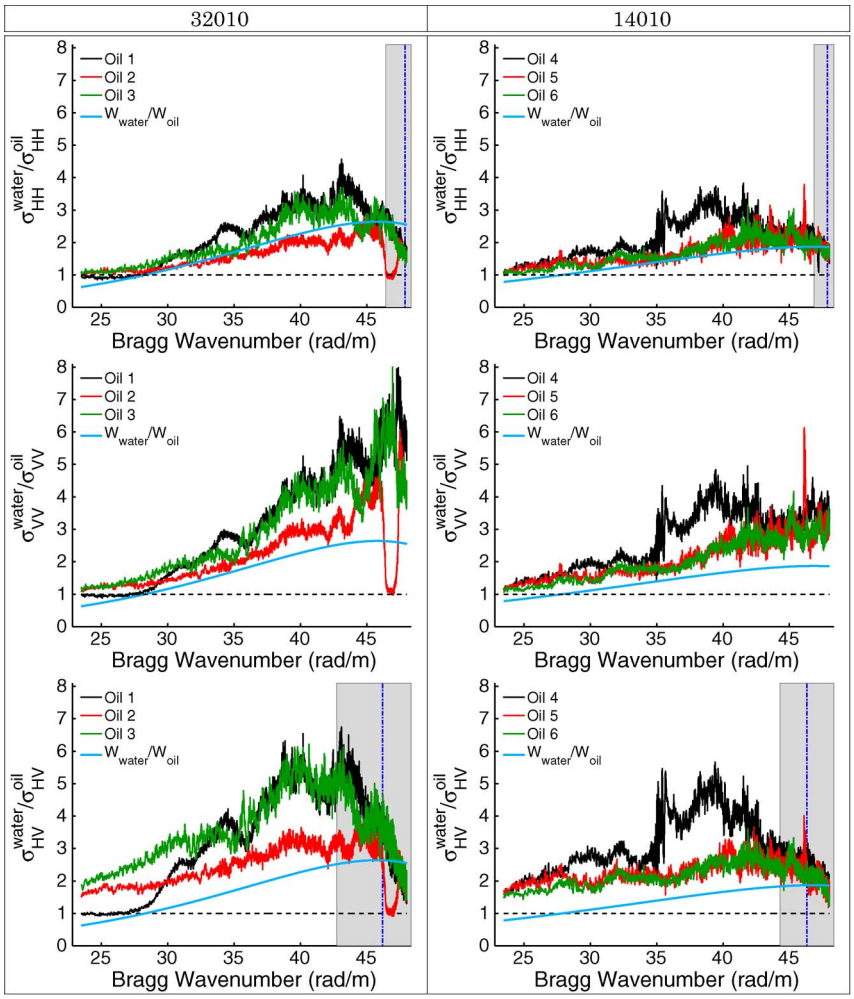

Fig. 10. Polarized damping ratios derived from multilooked UAVSAR data for flight tracks 32010 (left) and 14010 (right). The damping ratio of the ocean wave spectral density, W_{water}/W_{oil}, derived from the VV NCRS is shown in light blue.

damping ratios show a small dependence upon the polarization of the microwave radiation, with HH polarization damped less than the VV or HV returns at all Bragg wavenumbers below the SNR threshold, except at very low wavenumber (incidence angle), where the HV returns are most attenuated. The difference is small, ≈30%, but is outside of the reported relative calibration accuracy of 0.5 dB for the UAVSAR instrument. Given the small magnitude of the difference, further study of the instrument would be needed to validate the calibration before one would conclude that the observed polarization dependence of the damping ratios is a real measure of the surface scattering properties.

C. Eigenvalues of the Coherency Matrix

The major eigenvalue λ_1 (Fig. 11) is consistently lower for backscatter from oil than from water. This result is intuitive given that λ_1 is approximately equal to the total power return. Because the HV NRCS is only a small portion of the total backscatter power, λ_1 is relatively resilient to noise in the cross-

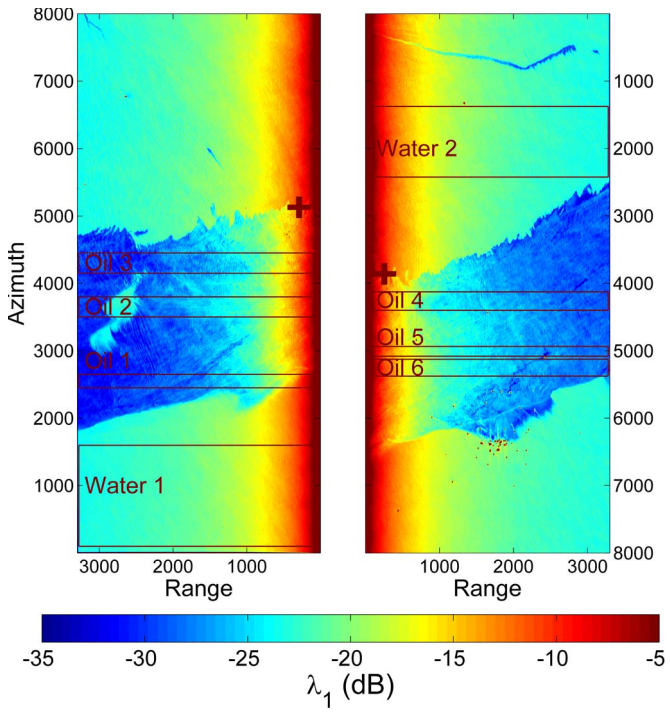

Fig. 11. Major eigenvalue (λ_1) images for 32010 (left) and 14010 (right) showing the four cross-track segments which are evaluated in further detail. The range and azimuth axes are in pixel units, with pixel size 7.2 m in azimuth and 5.0 m in slant range. The crosses locate a common point in the two overlapping images.

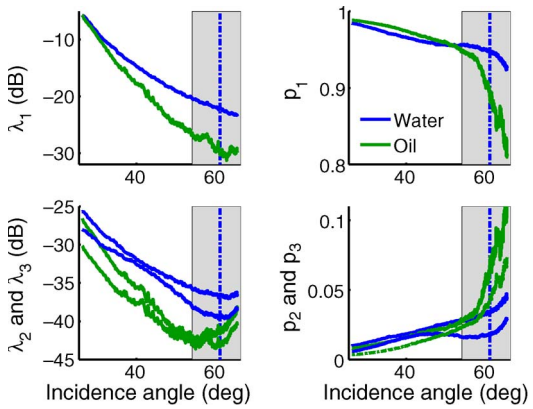

Fig. 12. Eigenvalues and pseudoprobabilities of T_3 for a representative oil (Oil 3) and water (Water 1) transect ($\lambda_1 \geq \lambda_2 \geq \lambda_3$). The gray shaded region indicates the region of the data where HV power over oil is within 6 dB of the instrument noise floor and the vertical blue dashed line indicates the incidence angle above which the HV power in the clear water data is within 6 dB of the instrument noise floor.

polarized channel, making it a potentially useful parameter for oil spill identification algorithms that are based on eigenvalue decomposition. Previous studies have shown that λ_1 can be used to image variations in the oil characteristics within the slick, which has been correlated with surface features observed with aerial imagery near the same time as the UAVSAR overflights [2].

Fig. 12 shows the eigenvalues and associated pseudoprobabilities for Oil 3 and Water 1. The major eigenvalue (upper left) and minor eigenvalues (lower left) are all lower for oil than for water across the entire range of accessible wavenumbers.

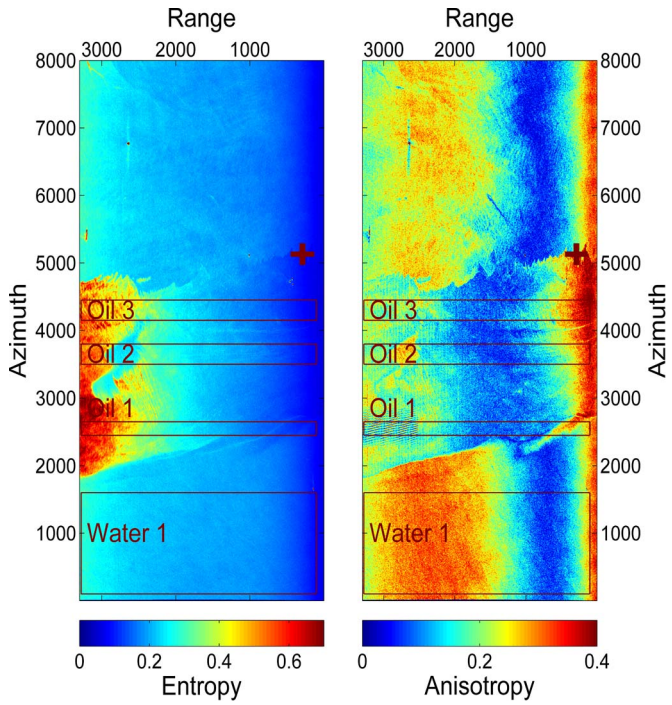

Fig. 13. Entropy (left) and anisotropy (right) for 32010 showing the four cross-track segments which are evaluated in further detail. The range and azimuth axes are in pixel units, with pixel size 7.2 m in azimuth and 5.0 m in slant range.

In fact, below approximately 50° AOI, the major eigenvalue for the oil in the slick has a higher pseudoprobability (Fig. 12, upper right) than the major eigenvalue for clean water adjacent to the slick. The only marked change in this behavior occurs at incidence angles where the HV backscatter power is below the SNR threshold (as indicated by the gray shaded area in Fig. 12). Therefore, we find that backscatter from clean water and the oil in the DWH slick are equally well described by the Bragg scattering mechanism. The only apparent exception occurs at high incidence angles where the instrument noise significantly affects the measured signal.

D. H/A/$\bar{\alpha}$ Decomposition

The results from the Cloude–Pottier H/A/$\bar{\alpha}$ decomposition provide further insight into the influence of a surface oil slick on backscatter from the ocean. Fig. 13 shows images of the entropy and anisotropy values in and around the main DWH slick derived from the data of line 32010. In Figs. 14–16, we show the along-track mean values of H, A, and $\bar{\alpha}$ for the segments of track 32010 defined in Table II, respectively.

The entropy values (Fig. 14 and left panel of Fig. 13) indicate that the scattering properties of both clean water and oil, derived from the UAVSAR data at all scattering angles over the entire UAVSAR scene, are consistent with a single scattering mechanism, namely Bragg scattering, for all measurements where the HV NRCS is above the SNR threshold. In each oil transect, the entropy values are consistently lower than those of the sea water at low to intermediate incidence angles. At approximately 48° AOI, the slope of the entropy with respect to the incidence angle over water flattens, causing the entropy values for the

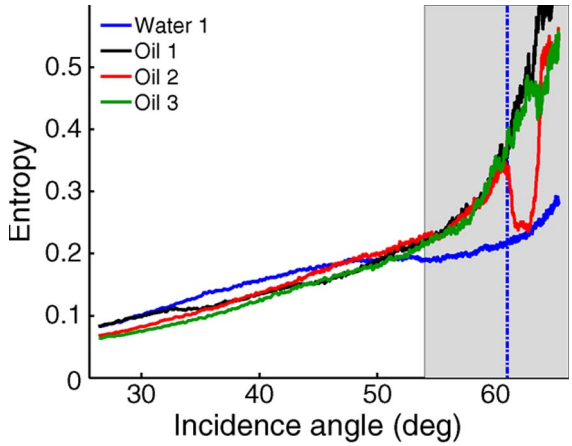

Fig. 14. Entropy for flight track 32010.

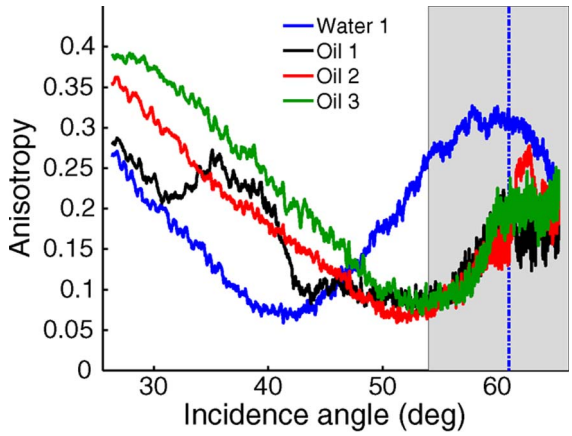

Fig. 15. Anisotropy for flight track 32010.

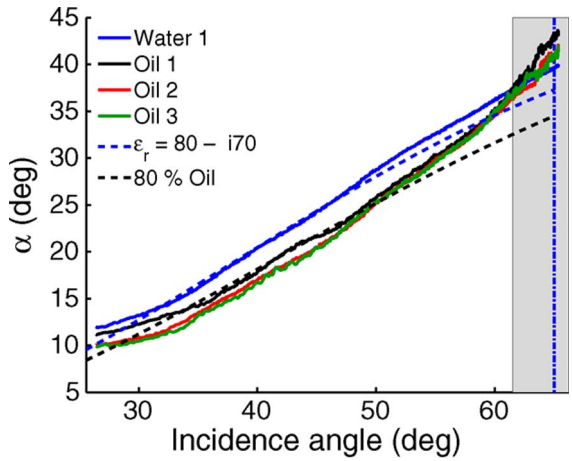

Fig. 16. Scattering parameter $\bar{\alpha}$ for flight track 32010. The theoretical values of $\bar{\alpha}$ calculated from the Bragg scatter coefficients [(20)] are also shown for sea water ($\varepsilon_r^{water} = 80 - i70$) and a mixture of 80% oil ($\varepsilon_r^{oil} = 2.3 - i0.02$) and 20% sea water.

oil lines to exceed those of water. This behavior manifests in the minor pseudoprobability values, p_2 and p_3, of water shown in Fig. 12 (blue lines, bottom right) where the slope of p_3 changes sign while the slope of p_2 remains constant. The area where the entropy values increase is evident in Fig. 13, where entropy at the far range has significantly higher values than oil or water at near range. This is where noise becomes a significant contribution to the measured signal.

The anisotropy values (Fig. 15 and right panel of Fig. 13) differ between oil and water and are incidence angle dependent. At low to intermediate incidence angles, oil has a higher anisotropy than water. This indicates that the surface is smoother in the areas contaminated by oil than in areas of relatively clean water, which is consistent with the analysis of the NRCS and corresponding theoretical NRCS calculated using the tilted Bragg model. The minimum anisotropy value is approximately the same for both oil and water, but occurs at different incident angle, i.e., at different Bragg wavelengths.

At intermediate incidence angles, the anisotropy values over water become greater than those over oil (the same result is seen in the 14010 data but at a slightly higher incidence angles), with the cross-over point in the range 43°–48°. This behavior is readily associated with the minor pseudoprobability values, where p_2 maintains a consistent slope and the sign of the slope of p_3 changes at approximately 48° AOI (Fig. 12, bottom right). The increase in the anisotropy values for oil at high incidence angles occurs when the HV NRCS over one of the oil lines is within 6 dB of the NESZ (gray shaded region). However, the HV NRCS for Oil 2 is higher than the NRCS for Oil 1 and Oil 3 (Fig. 7), so the HV return for Oil 2 is less corrupted by instrument noise than the other oil data. Since the anisotropy values at high incidence angles for Oil 2 begin increasing around 52° AOI, it is likely that in the absence of instrument noise, the anisotropy values for oil would behave in the same way as those for water, but with an incidence angle lag of approximately 10°, or a wavenumber change from 0.055 cm^{-1} to 0.065 cm^{-1} for the location of the minimum anisotropy.

It is known that for low entropy scatter, the anisotropy is highly affected by noise [44]. However, the anisotropy signal shows clear jumps between clean water and oil in the two segments that contain both, Oil 1 and Oil 2. The near range of Oil 1 contains clean water, and in this area, the anisotropy values track with the clean water line. The transition from water to oil in this segment occurs over a relatively diffuse boundary between approximately 30° and 35° AOI (range bins 300–600 in Fig. 6), with the higher anisotropy values between 35° and 40° AOI measured along the windward edge of the slick. In the Oil 1 segment, the decrease around 40° corresponds to where the transect moves into the interior of the slick. Although the anisotropy values of the oil are close to those of water around 45°, the backscatter remains much lower in the oil than in the adjacent clean water (Fig. 7). We think that this is due to variation in the incidence angle where the oil and water anisotropy curves cross and is probably attributable to variation in the slick properties, i.e., less concentrated oil or oil that has been affected by dispersants along the windward edge. As the incidence angle increases, the anisotropy for Oil 1 resembles the anisotropy of the other oil segments. Similar behavior is seen in Oil 2, where the jump from oil to water, which corresponds to the opening of clean water seen in Fig. 6, occurs between approximately 62° and 63° AOI. In the latter case, the data are noisy in the area of the transition due to the influence of instrument noise. These results suggest that the anisotropy values are not dominated by noise except in areas

that we explicitly show, but are measuring real properties of the scattering surface.

Over both water and oil, the scattering parameter, $\bar{\alpha}$, (Fig. 16) indicates a surface scatterer that is well described by Bragg scatter theory at low to intermediate incidence angles for sea water ($\varepsilon_r = 80 - i70$) and an 80% volumetric concentration of oil. In the DWH slick, we find that $\bar{\alpha}$ has little dependence on surface roughness. Rather, the difference between oil and water is due to the difference in the dielectric constant. Furthermore, the theory lines are calculated by assuming an untilted Bragg scatter model; their fit to the data indicates that $\bar{\alpha}$ is not significantly affected by moderate tilts of the ocean surface. At higher incidence angles, the $\bar{\alpha}$ values depart from the theoretical values and begin to converge to the same limit as the HH NRCS for oil approaches the instrument noise floor. The shaded region indicates the region where the HH NRCS for oil crosses the SNR threshold.

VII. Discussion

We have analyzed the L-band radar data acquired by the UAVSAR instrument over the main DWH slick in June 2010 and present results showing the difference between multipolarization backscatter and parameters of a polarimetric analysis in the oil relative to adjacent clean water. Our goal is to derive general information about the differences between radar backscatter from the main slick and from adjacent clean seawater.

A. Oil Slick Characterization

The NRCS for both water and oil and for all polarizations are well described by the tilted Bragg scattering model with sea surface RMS slope of 6.4° RMS for line 32010 and 7.2° for line 14010. The reduction in the NRCS between oil and water for each polarization was found to be caused by both the damping of the gravity-capillary waves and a change in the dielectric constant of the scattering medium. While it has been well documented in the literature that oil contaminated areas appear as areas of reduced NRCS, we discuss here how the behavior of oil and water differ as a function of incidence angle.

For intermediate and high incidence angle, the NRCS for each polarization clearly distinguishes oil and water. At low incidence angles, the co-polarized NRCS shows little difference between oil and water, a result that is predicted by the tilted Bragg theory for the given RMS slopes. On the other hand, the cross-polarized term indicates a greater difference between oil and water than the tilted Bragg model predicts, possibly because the HV NRCS is more sensitive to the RMS slope and dielectric constant than the co-polarized NRCS or because HV scattering is sensitive to scattering mechanisms that are not accounted for in the Bragg model.

Although we can distinguish oil in the DWH slick clearly from the surrounding clean water, our results indicate that for slicks on calm waters, even if the dielectric properties are known or estimated, differentiation between smooth water and oil is likely to be difficult using only the individual NRCS values. From our experience estimating the ocean surface RMS slope, we found that the VV NRCS is resilient to the tilt of the ocean surface; large tilt angles were needed to substantially displace the theoretical VV NRCS for water from the observed values.

Using the RMS slope angles that we determined from the co-polarized NRCS ratio of water, we determined the dielectric constant of the slick surface from the co-polarized NRCS ratios over oil and derive from it the volumetric concentration of oil in the water, assuming a layer thickness that is a significant fraction of the skin depth of the microwave radiation. We estimated the volumetric concentration of oil in the vicinity of DWH to be approximately 80%, a result that is generally supported by the aerial *in situ* observations of oil emulsion throughout the main slick but is difficult to verify without additional *in situ* observations. Our analysis indicated a range in concentrations from 65% to 90% across the spill. These results are consistent with a mixed layer several millimeters thick of oil entrained with seawater in the main part of the DWH slick, where new oil was surfacing constantly from the release at the sea floor.

In these data, the damping ratio for the thick surface oil layer does not measure the ocean wave spectrum damping alone, but a combination of the wave spectral change and a dielectric change in the upper surface layer. We find that the damping ratios over the slick show larger values than the ratio of the ocean wave spectra alone predict. We attribute this difference to the change in the dielectric properties in the scattering medium. Variations in the damping ratio within the slick are clearly discernible, indicating a sensitivity to the surface oil characteristics, including concentration, form, and thickness. One unknown factor that may result in varying returns is the application of dispersants to the surface oil. Further study of these variations is warranted to learn more about oil characterization with L-band radar.

The major eigenvalue of the coherency matrix, λ_1, readily distinguishes oil from water above 35° AOI. As with the NRCS, λ_1 over oil decreases relative to the water as the incidence angle increases. Because in cases where there is a single dominant scatterer, λ_1 is approximately equivalent to the trace of the coherency matrix, the co-polarized terms dominate, and the instrument noise induced on the cross-polarized term has little effect. The result is that λ_1 is a relatively robust oil identification parameter. Furthermore, the coherency matrix T_3 is linearly related to the 3×3 covariance matrix, whose diagonal components are the NRCS for each polarization channel (HV NRCS is multiplied by 2), meaning that they have the same eigenvalues and trace. Therefore, λ_1 can be calculated as the sum of the NRCS values. Over the ocean, the HV NRCS is much lower than the co-polarized NRCS, so that λ_1 can be easily approximated as the sum of the co-polarized NRCS, which is computationally much simpler than performing a polarimetric decomposition.

We find that L-band backscatter from both oil and water consistently shows the backscatter mechanism to be Bragg backscatter from a tilted faceted surface, with surface scattering being the dominant type of backscatter. At incidence angles less than 50°, oil shows a more dominant single scatterer than water, albeit with significantly lower scattered power.

In the main DWH slick, entropy values were low, consistent with Bragg scattering and comparable to entropy values over clean water, differing by <0.05 where all NRCS data were above the SNR threshold. Entropy values over oil are lower than those over clean water at incidence angles below approximately 50° and higher than clean water at higher incidence angles. Entropy values over oil are higher above 50° AOI because the slope of the entropy values over water flattens at approximately 45° AOI. The physics of this process is unknown, and this result indicates that oil spill identification with entropy is problematic. We note that [2] found the entropy values to be high, close to unity, for weathered oil from the spill that moved into Barataria Bay. As discussed below, this is likely due to the effect of instrument noise on the low signal return from the oiled bay waters, which had a thin sheen film at the time of the UAVSAR data acquisition.

Analysis of the anisotropy data yields results that are inconsistent with previous findings. Using Airborne Synthetic Aperture Radar (AIRSAR) data acquired off the coast of Southern California, Schuler and Lee found that anisotropy values for biogenic films have no range dependence [47]. Our results do not support the same conclusion, as we observe a clear range (incidence angle) dependence over both clean water and the DWH mineral slick. Systematic and repeated trends are also evident as are jumps between oil and water values whenever the respective transect crosses the edge of the slick. The disparity between our results and those of [47], while possibly due to slick type, could also be due to the lower noise floor inherent in the UAVSAR instrument as compared to AIRSAR, as discussed in Section VII-B.

B. Influence of Instrument Noise

Radar backscatter is low from oil slicks, calm wind areas, and other oil look-alikes and is therefore more likely to be close to the instrument noise floor than backscatter from most other media. The cross-polarized backscatter is particularly susceptible to corruption from instrument noise because the cross-polarized NRCS is generally much lower than the co-polarized NRCS. As a result, any analysis of oil spills, biogenic slicks, or other low-backscatter areas must take into account the values of the NRCS for each polarization channel relative to the NESZ of the instrument.

Our analyses show that the UAVSAR instrument noise is a small component of the signal at incidence angles less than 55° for HV returns and less than 62° for HH returns. An independent analysis based on noise filtering confirmed the low noise in the data (Appendix B).

Close proximity to the instrument noise floor in any of the NRCS channels has a profound effect on the eigenvalues and their associated parameters. This is most clear in the pseudo-probabilities and the entropy. When the HV NRCS is within 6 dB of the NESZ, the entropy values increase rapidly, and the values of the pseudoprobabilities converge due to the randomness in the instrument noise. The variance in the anisotropy has a higher magnitude and frequency whenever the HV NRCS is close to the noise floor.

Our results for entropy conflict with those of a previous study. In [47], the entropy for biogenic slicks was shown to be high at incidence angles above 45° and was interpreted as an indication of a high degree of randomness in the slick covered areas. This phenomena were ascribed to damping of the ambient-level Bragg scatter and the existence of multiple scatterers of comparable strength. The authors analyze the co-polarized phase difference and observe the behavior of the eigenvalues in order to demonstrate that the data they used are above the system noise floor. The authors state that because the major eigenvalue decreases while the minor eigenvalues increase as a given transect encounters a slick, the data are above the instrument noise floor. Our results, shown in Fig. 12, show that the eigenvalues for oil in the DWH slick are always lower than the respective eigenvalues for water, even when the HV NRCS for both water and oil are within 6 dB of the instrument noise floor. We find that all eigenvalues derived from data with HV and HH NRCS near the noise floor show a notable change when transitioning from water to oil. Furthermore, in Appendix B, we show that the symmetry of the co-polarized phase difference, which the authors of [47] also use to evaluate the proximity of the backscatter to the instrument noise floor, is independent of the noise level in the HV backscatter and therefore an inappropriate gauge of the noise level in HV polarimetric backscatter. Finally, our analysis of the entropy shows a comparable increase in the entropy values above 54° AOI, where the HV NRCS is close to the noise floor. Athough the two studies do not analyze the same type of slick, given that UAVSAR has a lower noise floor than AIRSAR, we find that it is possible that the results in [47] for the observed $\mathrm{H/A}/\bar{\alpha}$ values at higher incidence angles are due to instrument noise.

VIII. Conclusion

We find the general result that L-band radar backscatter from both oil and water in moderate wind conditions are well described by the tilted Bragg model across the range of incidence angles from 26° to 60°, with the backscatter from oil being even more strongly governed by surface scattering from a single dominant scatter than backscatter from water for incidence angles below 50°. From the combination of co-polarized and cross-polarized NRCSs and their ratios analyzed over water and oil, we show that for the DWH slick, the change in backscatter was due to both a damping of the ocean wave spectral components by the oil and a reduction in the effective dielectric constant of the surface. From the reduction, we estimate that the upper layer of the oil slick was a mixture of approximately 80% oil and 20% sea water, with a range in the oil volumetric concentration from 65% to 90% across the observed area of the slick. This is an important new observation because the effective dielectric constant can provide valuable information to help distinguish thick oil layers from areas with thin films of mineral oil or other natural, or lower priority, surface contaminants and from clean water areas with smaller wind effects.

Our polarimetric decomposition using the $\mathrm{H/A}/\bar{\alpha}$ parameters shows a dominant scatterer for both water and oil, consistent with a Bragg scatterer. For the DWH oil slick, we find no

significant contribution from a non-Bragg scatterer, although we note that at the highest incidence angles, instrument noise could be misinterpreted as such. These results differ from those of [29], [30]. Our decomposition shows there to be small but statistically significant contributions from secondary scatterers for both oil and water. All three eigenvalues of the decomposition were consistently less for oil than water over the entire observed range of incidence angles, indicating overall reduced backscatter from all scatterers. The major eigenvalue of the decomposition distinguishes oil from water at all but the lowest incidence angles and shows little change when noise is a major component of the backscatter in only the HV channel, making it the most reliable indicator of the main slick. This eigenvalue is approximately equal to the total backscatter power over both oil and water and can be accurately estimated from the HH and VV NRCS alone, a computationally efficient alternative to eigenvalue decomposition. Although the H/A/$\bar{\alpha}$ parameters have been used previously to classify slicks on the ocean surface [47], we find that for this mineral oil slick, the entropy and alpha parameters are comparable to those for clean sea water. Although small in all cases, the entropy values for oil are lower than those for water at low to intermediate incidence angles, but higher than water at higher incidence angles. Through a detailed noise analysis, we find that the results from the previous study are consistent with contamination by instrument noise. We show that anisotropy has the same general characteristics for oil and water, but with a shift in the Bragg wavenumber of the minimum anisotropy.

We conclude from this study of DWH oil that the H/A/$\bar{\alpha}$ parameters are likely to be beneficial to oil slick classification only when using low noise instruments. The entropy for either oil or water increases substantially only as the NRCS approaches the noise floor. Below this point, the difference in entropy between oil and water is relatively small. We conclude that the apparent randomness implied by the increasing entropy is due to randomness of the instrument noise and should not be considered indicative of the physics of the scattering mechanism. The anisotropy shows substantial variation across the oil slick, indicating possible sensitivity to oil characteristics. We observe a significant range dependence in the anisotropy whenever the backscatter in all channels is more than 6 dB above the instrument noise floor. Further study is warranted to validate these results.

This study shows that a low noise L-band quad-polarization SAR can be used to not only detect oil slicks but to characterize to some extent the oil within the slick, as we showed by determining a volumetric oil concentration in the slick using a fit to the tilted Bragg model. The results show general trends with variations within the slick that warrant further study of oil classification using this type of instrument.

APPENDIX A
UAVSAR NOISE EQUIVALENT SIGMA-ZERO

The magnitude of the NESZ depends on the transmitted power, antenna gain, system losses, and operating temperature of the radar instrument. As a result, the NESZ is instrument specific, varies as a function of incidence angle, and is on average polarization independent. The UAVSAR NESZ is measured by operating the instrument in receive-only mode and processing the receive-only ("sniffer") data to obtain an equivalent normalized cross section. The NESZ determined in this way incorporates the additive noise of the instrument and the multiplicative noise from data quantization and impulse sidelobes. The additive instrument noise component of the NESZ is Gaussian white noise and differs from pulse to pulse for horizontal and vertical receive polarizations because the two are collected at different times.

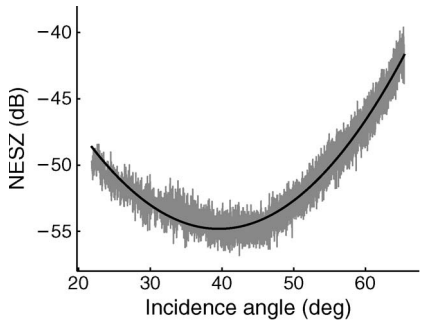

Fig. 17. Noise equivalent sigma zero for UAVSAR flight track gulfco_32010_10054_101_100623 (referred to as 32010 in this study) collected 23-June-2010.

We evaluate the UAVSAR NESZ for the data used in this study using the sniffer pulses collected once every 756 pulses (≈0.6 Hz) in line 32010 concurrently with the science data over the main DWH slick. We extracted these sniffer pulses from the raw data, randomized their along-track ordering so that the data would be decorrelated during azimuth compression, and processed the sniffer pulses using the UAVSAR processing suite. We calculated the mean NESZ as a function of incidence angle from 100 randomly selected processed pulses and fit a fourth-order polynomial to the data (Fig. 17). The best-fit coefficients are given in Table III. The NESZ for line 32010 is consistent with previously published values for the UAVSAR NESZ [2].

APPENDIX B
RESIDUAL NOISE EVALUATION AND FILTERING

The noise filtering method outlined in [49] was adopted to evaluate and remove the noise that remained in the data after crosstalk calibration, the standard 3 × 12 (range × azimuth) UAVSAR multilooking, and averaging the coherency matrix over a 9 × 9 window. This method considers the difference between the HV and VH backscattered power to be indicative of the residual noise level in the system because, in the absence of noise, the cross-polarized return should be identical in a monostatic radar system due to reciprocity. Because the HV and VH data are averaged and delivered as only HV data in the standard UAVSAR products, we had to reprocess the raw UAVSAR data to test this noise filtering method.

For residual noise filtering, we proceed by forming the 4 × 4 coherency matrix as [43], [49]

$$\langle \mathbf{T}_4 \rangle = \left\langle \mathbf{k}_4 \mathbf{k}_4^{*T} \right\rangle \tag{21}$$

TABLE III
BEST-FIT COEFFICIENTS FOR UAVSAR NESZ

x	c_4	c_3	c_2	c_1	c_0
Slant range (km)	1.2921×10^{-3}	-0.1221	4.2780	-64.7770	302.1079
Incidence angle (deg)	0	0	1.9664×10^{-2}	-1.5561	-24.0269

$$NESZ(dB) = c_4x^4 + c_3x^3 + c_2x^2 + c_1x + c_0$$

where

$$\mathbf{k}_4 = \frac{1}{\sqrt{2}}\begin{bmatrix} S_{HH}+S_{VV} \\ S_{HH}-S_{VV} \\ S_{HV}+S_{VH} \\ i(S_{HV}-S_{VH}) \end{bmatrix}. \tag{22}$$

Eigenvalue decomposition can be applied to T_4 in the same manner as it is applied to T_3. In the presence of noise, T_4 has real, nonnegative eigenvalues $\lambda_1 \geq \lambda_2 \geq \lambda_3 \geq \lambda_4 > 0$ and, in the case of a single dominant scatterer, $\lambda_1(T_4) \approx \lambda_1(T_3)$. The smallest eigenvalue of T_4 is defined to be the average noise power σ_n[49]. It is clear from (22) that if $S_{HV} = S_{VH}$, T_4 reduces to T_3.

The averaged noise power, which is assumed to be the same in all polarization channels, can be removed by subtracting the noise-equivalent coherency matrix, T_n, from the 3×3 coherency matrix

$$\langle \mathbf{T}_{3_f} \rangle = \langle T_3 \rangle - \langle T_n \rangle \tag{23}$$

where T_{3_f} is the filtered coherency matrix and the noise-equivalent coherency matrix is

$$\langle \mathbf{T}_n \rangle = \sigma_n \mathbf{I} \tag{24}$$

where $\mathbf{I}$ is the identity matrix [49]. The eigenvector decomposition can then proceed as described in Section II-B.2 using T_{3_f} in place of T_3. An alternative to removing the noise via (23) is to simply subtract λ_4 from the eigenvalues of T_3[43].

As shown in Fig. 5, the noise calculated with this filtering method contributes very little to overall power, which in the case of scatter from the ocean is primarily described by the largest eigenvalue λ_1. As a result, subtracting λ_4 from the eigenvalues has a non-negligible effect on only λ_2 and λ_3. For the data used in this study, the effect of the noise filtering is relatively small and occurs only at low and high incidence angles (Fig. 18). We can also see in Fig. 18 that applying the filtering procedure scales the oil and water values of λ_2 and λ_3 by approximately the same amount. This means that the filtering process described here will only change the absolute values of the H/A/$\bar{\alpha}$ parameters, not the relative values of oil and water. As is expected from the analysis of λ_2 and λ_3, the entropy and anisotropy calculated from the filtered coherency matrix differ in absolute value from those calculated using the unfiltered coherency matrix (Fig. 18). The relative values of oil and water remain approximately the same with or without filtering, though the difference in anisotropy at low incidence angle between oil and water is more pronounced after filtering. When the data are near the instrument noise floor, the filtering process only scales the value down for entropy and up for anisotropy but the variance in each appears to be unaffected by filtering. This shows that this filtering method does not fully remove the instrument noise, which is channel independent.

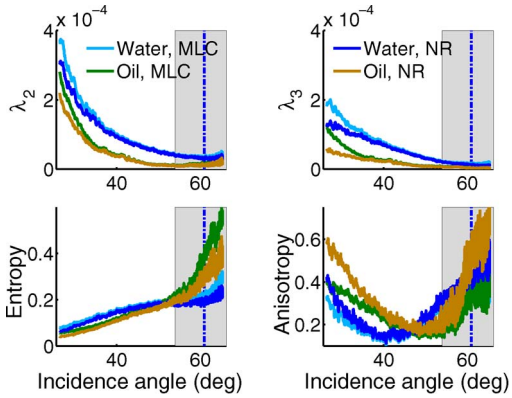

Fig. 18. Second and third eigenvalues, entropy, and anisotropy of the standard UAVSAR multilooked cross product (MLC) data and the noise reduced (NR) coherency matrices for representative oil (Oil 3) and water (Water 1) tracks.

Another method that has been used to evaluate noise in oil slick studies utilizes the co-polarized phase difference. In [47], the authors observe the co-polarized phase difference, $Arg(S_{HH}S^*_{VV})$, and conclude that the signals they observe are above the noise floor because the distribution of the co-polarized phase is symmetric about zero. This conclusion motivates a brief discussion of the co-polarized phase difference ϕ_c and its behavior in the presence of known noise. Numerous processed return pulses (range lines) from the Water 1 and Oil 1 segments were analyzed and the mean, standard deviation, and skewness of ϕ_c were calculated using a 9×9 moving window over each segment prior to the analysis of individual lines. One randomly selected range line from each segment and the moments of the statistical distribution are shown in Fig. 19. The skewness is calculated as

$$s(\phi_c) = b\frac{\frac{1}{n}\sum_{i=1}^{n}(\phi_{c_i}-\mu)^3}{\left(\frac{1}{n}\sum_{i=1}^{n}(\phi_{c_i}-\mu)^2\right)^3} \tag{25}$$

where $n = 81$, μ is the mean, σ is the standard deviation, and b is the bias correction

$$b = \frac{\sqrt{n(n-1)}}{n-2}. \tag{26}$$

From this evaluation, we conclude that ϕ_c is not a suitable parameter for evaluating the proximity of the polarimetric data to the instrument noise floor. We find that there is no discernible change in the characteristics of ϕ_c over oil as the HV oil data

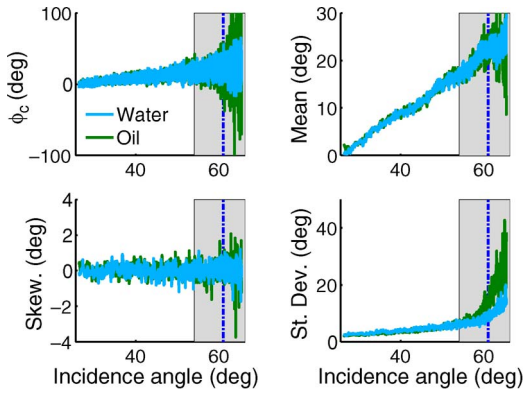

Fig. 19. Co-polarized phase difference ϕ_c for representative oil (Oil 3) and water (Water 1) range line. The upper left panel is ϕ_c for one randomly selected range line in each track. The mean value in the upper right panel, the skewness in the lower left panel, and the standard deviation in the lower right panel are calculated over a 9×9 moving window. The shaded area indicates the incidence angles at which the power of the HV scatter over oil is less than the SNR threshold of 6 dB above the instrument noise floor and the vertical blue dotted line indicates that the power of the HV scatter over water is within 6 dB of the noise floor. The power of the HH return over oil crossed the SNR threshold at 62° AOI.

cross the SNR threshold and that ϕ_c has nonzero mean value at all incidence angles, with the mean of ϕ_c increasing linearly with incidence angle. The only prominent changes in ϕ_c and its moments occur at incidence angles above where the HH oil data cross the noise threshold. Because power of the HV data collected over the ocean in low-to-moderate wind should always be lower than the power in both of the co-polarized returns, ϕ_c could remain unchanged even when instrument noise is a non-negligible component of the cross-polarized scatter. It is also worth noting that we find in the UAVSAR data virtually no difference between the standard deviation of ϕ_c for oil and for water except in the presence of instrument noise.

ACKNOWLEDGMENT

The research described in this paper was carried out at the Jet Propulsion Laboratory (JPL), California Institute of Technology, under a contract with the National Aeronautics and Space Administration. The UAVSAR data are processed by the UAVSAR team at JPL and archived for open distribution at the Alaska Satellite Facility. The authors would like to acknowledge C. Dobson, NASA Headquarters, for endorsing the UAVSAR flights; and S. Hensley, JPL, I. Leifer, University of Santa Barbara, and I. MacDonald and O. Garcia-Pineda, Florida State University, for valuable discussions. Thanks are also extended to B. Hawkins, Y. Zheng, and B. Chapman, JPL. The third author would also like to acknowledge the DESDynl Pre-mission Task for support. This paper is Caltech Seismo Lab contribution 10055.

REFERENCES

[1] T. J. Crone and M. Tolstoy, "Magnitude of the 2010 Gulf of Mexico oil leak," *Science*, vol. 330, no. 6004, p. 634, Oct. 2010.

[2] C. E. Jones, B. Minchew, B. Holt, and S. Hensley, "Studies of the Deepwater Horizon oil spill with the UAVSAR radar," in *Monitoring and Modeling of the Deepwater Horizon Oil Spill: A Record-Breaking Enterprise*, Y. Liu, A. MacFadyen, Z.-G. Ji, and R. H. Weisberg, Eds. Washington, DC: Amer. Geophys. Union, 2011, pp. 33–50.

[3] E. Ramsey III, A. Rangoonwala, Y. Suzuoko, and C. Jones, "Oil detection in coastal marsh with polarimetric synthetic aperture radar (SAR)," *Remote Sens.*, vol. 3, no. 12, pp. 2630–2662, Dec. 2011.

[4] M. Fingas and C. Brown, "Review of oil spill remote sensing," *Spill Sci. Techn. Bull.*, vol. 4, no. 4, pp. 199–208, 1997.

[5] K. Folgerø, "Bilinear calibration of coaxial transmission/reflection cells for permittivity measurement of low-loss liquids," *Meas. Sci. Technol.*, vol. 7, no. 9, pp. 1260–1269, Sep. 1996.

[6] T. Friiso, Y. Schildberg, O. Rambeau, T. Tjomsland, H. Førdedal, and J. Sjøblom, "Complex permittivity of crude oil and solutions of heavy crude oil fractions," *J. Dispers. Sci. Technol.*, vol. 19, no. 1, pp. 93–126, 1998.

[7] F. T. Ulaby, R. K. Moore, and A. K. Fung, *Microwave Remote Sensing: Active and Passive*. Dedham, MA: Artech House, 1986.

[8] H. Espedal, O. Johannessen, J. Johannessen, E. Dano, D. Lyzenga, and J. Knulst, "COASTWATCH'95: ERS 1/2 SAR detection of natural film on the ocean surface," *J. Geophys. Res.*, vol. 103, no. C11, pp. 24 969–24 982, Oct. 1998.

[9] H. A. Espedal and T. Wahl, "Satellite SAR oil spill detection using wind history information," *Int. J. Remote Sens.*, vol. 20, no. 1, pp. 49–65, Jan. 1999.

[10] V. Wismann, M. Gade, W. Alpers, and H. Hühnerfuss, "Radar signatures of marine mineral oil spills measured by an airborne multi-frequency radar," *Int. J. Remote Sens.*, vol. 19, no. 18, pp. 3607–3623, 1998.

[11] T. Wahl, A. Skoelv, T. Anderssen, J. Pedersen, J. Andersen, O. Follum, G. Strom, T. Bern, H. Hamnes, and T. Solberg, "Radar satellites: A new tool for pollution monitoring in coastal waters," *Coastal Manage.*, vol. 24, no. 1, pp. 61–71, 1996.

[12] M. A. Donelan and W. J. Pierson, "Radar scattering and equilibrium ranges in wind-generated waves with application to scatterometry," *J. Geophys. Res.*, vol. 92, no. c5, pp. 4971–5029, 1987.

[13] W. Alpers and H. Hühnerfuss, "Radar signatures of oil films floating on the sea surface and the Marangoni effect," *J. Geophys. Res.*, vol. 93, no. C4, pp. 3442–3648, 1988.

[14] M. Gade, W. Alpers, H. Hühnerfuss, V. Wismann, and P. Lange, "On the reduction of the radar backscatter by oceanic surface films: Scatterometer measurements and their theoretical interpretation," *Remote Sens. Environ.*, vol. 66, no. 1, pp. 52–70, Oct. 1998.

[15] M. Gade, W. Alpers, H. Hühnerfuss, H. Masuko, and T. Kobayashi, "Imaging of biogenic and anthropogenic ocean surface films by the multifrequency/multipolarization SIR-C/X-SAR," *J. Geophys. Res.*, vol. 103, no. C9, pp. 18 851–18 866, 1998.

[16] S. Ermakov, "On the intensification of decimeter-range wind waves in film slicks," *Izvestiya, Atmos. Ocean. Phys.*, vol. 46, no. 2, pp. 208–213, Apr. 2010.

[17] A. Solberg, G. Sotrvik, R. Solberg, and E. Volden, "Automatic detection of oil spills in ERS SAR images," *IEEE Trans. Geosci. Remote Sens.*, vol. 37, no. 4, pp. 1916–1924, Jul. 1999.

[18] F. Girard-Ardhuin, G. Mercier, F. Collard, and R. Garello, "Operational oil-slick characterization by SAR imagery and synergistic data," *IEEE J. Ocean. Eng.*, vol. 30, no. 3, pp. 487–495, Jul. 2005.

[19] B. Fiscella, A. Giancaspro, F. Nirchio, P. Pavese, and P. Trivero, "Oil spill detection using marine SAR images," *Int. J. Remote Sens.*, vol. 21, no. 18, pp. 3561–3566, 2000.

[20] C. Brekke and A. Solberg, "Classifiers and confidence estimation for oil spill detection in ENVISAT ASAR images," *IEEE Geosci. Remote Sens. Lett.*, vol. 5, no. 1, pp. 65–69, Jan. 2008.

[21] F. Del Frate, A. Petrocchi, J. Lichtenegger, and G. Calabresi, "Neural networks for oil spill detection using ERS-SAR data," *IEEE Trans. Geosci. Remote Sens.*, vol. 38, no. 5, pp. 2282–2287, Sep. 2000.

[22] A. Y. Ivanov and V. V. Zatyagalova, "A GIS approach to mapping oil spills in a marine environment," *Int. J. Remote Sens.*, vol. 29, no. 21, pp. 6297–6313, Nov. 2008.

[23] O. Garcia-Pineda, B. Zimmer, M. Howard, W. Pichel, X. Li, and I. MacDonald, "Using SAR images to delineate ocean oil slicks with a texture-classifying neural network algorithm (TCNNA)," *Can. J. Remote Sens.*, vol. 35, no. 5, pp. 411–421, Oct. 2009.

[24] A. Gambardella, G. Giacinto, M. Migliaccio, and A. Montali, "One-class classification for oil spill detection," *Pattern Anal. Appl.*, vol. 13, no. 3, pp. 349–366, Aug. 2010.

[25] Y. Shu, J. Li, H. Yousif, and G. Gomes, "Dark-spot detection from SAR intensity imagery with spatial density thresholding for oil-spill monitoring," *Remote Sens. Environ.*, vol. 114, no. 9, pp. 2026–2035, Sep. 2010.

[26] P. Trivero, B. Fiscella, F. Gomez, and P. Pavese, "SAR detection and characterization of sea surface slicks," *Int. J. Remote Sens.*, vol. 19, no. 3, pp. 543–548, Feb. 1998.

[27] M. Migliaccio, F. Nunziata, and A. Gambardella, "On the copolarised phase difference for oil spill observation," *Int. J. Remote Sens.*, vol. 30, no. 6, pp. 1587–1602, Jan. 2009.
[28] F. Nunziata, P. Sobieski, and M. Migliaccio, "The two-scale BPM scattering model for sea biogenic slicks contrast," *IEEE Trans. Geosci. Remote Sens.*, vol. 47, no. 7, pp. 1949–1956, Jul. 2009.
[29] F. Nunziata, A. Gambardella, and M. Migliaccio, "On the Mueller scattering matrix for SAR sea oil slick observation," *IEEE Trans. Geosci. Remote Sens.*, vol. 5, no. 4, pp. 691–695, Oct. 2008.
[30] M. Migliaccio, A. Gambardella, F. Nunziata, and M. Shimada, "The PALSAR polarimetric mode for sea oil slick observation," *IEEE Trans. Geosci. Remote Sens.*, vol. 47, no. 12, pp. 4032–4041, Dec. 2009.
[31] R. N. Clark, G. A. Swayze, I. Leifer, K. E. Livo, R. Kokaly, T. Hoefen, S. Lundeen, M. Eastwood, R. O. Green, N. Pearson, C. Sarture, I. McCubbin, D. Robers, E. Bradley, D. Steele, T. Ryan, and R. Dominguez, "A method for quantitative mapping of thick oil spills using imaging spectroscopy," U.S. Geological Survey, Menlo Park, CA, Tech. Rep. 1167, 2010, Open-File Report 2010-1167.
[32] G. R. Valenzuela, "Theories for the interaction of electromagnetic and ocean waves—A review," *Boundary-Layer Meteorol.*, vol. 13, no. 1–4, pp. 61–85, Jan. 1978.
[33] J. Wright, "Backscattering from capillary waves with application to sea clutter," *IEEE Trans. Antennas Propag.*, vol. AP-14, no. 6, pp. 749–754, Nov. 1966.
[34] G. R. Valenzuela, "Scattering of electromagnetic waves from a tilted slightly rough surface," *Radio Sci.*, vol. 3, no. 6, pp. 1057–1066, 1968.
[35] G. R. Valenzuela, M. B. Laing, and J. C. Daley, "Ocean spectra for the high frequency waves as determined from airborne radar measurements," *J. Marine Res.*, vol. 29, pp. 69–84, 1971.
[36] J. Wright, "A new model for sea clutter," *IEEE Trans. Antennas Propag.*, vol. AP-16, no. 2, pp. 217–223, Mar. 1968.
[37] E. H. Harvey, "The surface tension of crude oils," *Ind. Eng. Chem*, vol. 17, no. 1, p. 85, Jan. 1925.
[38] O. M. Phillips, "On the generation of waves by turbulent wind," *J. Fluid Mech.*, vol. 2, no. 5, pp. 417–445, 1957.
[39] D. B. Creamer and J. A. Wright, "Surface films and wind wave growth," *J. Geophys. Res.*, vol. 97, no. C4, pp. 5221–5229, 1992.
[40] M. Longuet-Higgins, "On wave breaking and the equilibrium spectrum of wind-generated waves," *Proc. R. Soc. Lond.*, vol. 310, no. 1501, pp. 151–159, May 1969.
[41] E. W. North, E. E. Adams, Z. Schlag, C. R. Sherwood, R. He, K. H. Hyun, and S. A. Socolofsky, "Simulating oil droplet dispersal from the Deepwater Horizon spill with a Lagrangian approach," in *Monitoring and Modeling of the Deepwater Horizon Oil Spill: A Record-Breaking Enterprise*, Y. Liu, A. MacFadyen, Z.-G. Ji, and R. H. Weisberg, Eds. Washington, DC: Amer. Geophys. Union, 2011, pp. 217–226.
[42] S. R. Cloude, "Group theory and polarization algebra," *Optik*, vol. 75, no. 1, pp. 26–36, 1986.
[43] S. R. Cloude and E. Pottier, "A review of target decomposition theorems in radar polarimetry," *IEEE Trans. Geosci. Remote Sens.*, vol. 34, no. 2, pp. 498–518, Mar. 1996.
[44] S. R. Cloude and E. Pottier, "An entropy based classification scheme for land applications of polarimetric SAR," *IEEE Trans. Geosci. Remote Sens.*, vol. 35, no. 1, pp. 68–78, Jan. 1997.
[45] J.-S. Lee and E. Pottier, *Polarimetric Radar Imaging: From Basics to Applications*. Boca Raton, FL: CRC Press, 2009.
[46] S. R. Cloude and K. P. Papathanassiou, "Polarimetric SAR interferometry," *IEEE Trans. Geosci. Remote Sens.*, vol. 36, no. 5, pp. 1551–1565, Sep. 1998.
[47] D. Schuler and J. Lee, "Mapping ocean surface features using biogenic slick fields and SAR polarimetrc decomposition techniques," *Proc. Inst. Elect. Eng.—Radar, Sonar Navig.*, vol. 153, no. 3, pp. 260–270, Jun. 2006.
[48] M. Migliaccio, A. Gambardella, and M. Tranfaglia, "SAR polarimetry to observe oil spills," *IEEE Trans. Geosci. Remote Sens.*, vol. 45, no. 2, pp. 506–511, Feb. 2007.
[49] I. Hajnsek, E. Pottier, and S. Cloude, "Inversion of surface parameters from polarimetric SAR," *IEEE Trans. Geosci. Remote Sens.*, vol. 41, no. 4, pp. 727–744, Apr. 2003.
[50] D. Schuler, J. Lee, and D. Kasilingam, "Polarimetric SAR techniques for remote sensing of ocean surface," in *Signal and Image Processing for Remote Sensing*, C. Chen, Ed. New York: Taylor & Francis, 2006, pp. 267–304.
[51] NOAA, NOAA Office of Response and Restoration Open water oil identification Job Aid for Aerial Observation2007. [Online]. Available: http://response.restoration.noaa.gov/jobaid/orderform, NOAA Office of Response and Restoration
[52] S. Hensley, Y. Lou, P. Rosen, K. Wheeler, H. Zebker, S. Madsen, T. Miller, J. Hoffman, and D. Farra, "An L-band SAR for repeat pass deformation measurements on a UAV platform," presented at the Proc. 2nd AIAA 'Unmanned Unlimited Systems, Technol., Oper.-Aerospace, San Diego, CA, 2003, Paper AIAA 2003-6619.
[53] A. Freeman and S. Durden, "A three-component scattering model for polarimetric SAR data," *IEEE Trans. Geosci. Remote Sens.*, vol. 36, no. 3, pp. 963–973, May 1998.
[54] C. Lopez-Martinez, E. Pottier, and S. Cloude, "Statistical assessment of eigenvector-based target decomposition theorems in radar polarimetry," *IEEE Trans. Geosci. Remote Sens.*, vol. 43, no. 9, pp. 2058–2074, Sep. 2005.
[55] J. Lee, T. Ainsworth, J. Kelley, and C. Lopez-Martinez, "Evaluation and bias removal of multilook effect on entropy/alpha/anisotropy in polarimetric SAR decomposition," *IEEE Trans. Geosci. Remote Sens.*, vol. 46, no. 10, pp. 3039–3052, Oct. 2008.

Brent Minchew received the B.S. and M.S.E. degrees in aerospace engineering from the University of Texas at Austin, Austin, in 2008 and 2010, respectively. He is currently working toward the Ph.D. degree in geophysics at the California Institute of Technology, Pasadena.

His current research focuses primarily on glaciers with particular emphasis on remote sensing techniques. During summer 2009 and summer 2010, he was a Graduate Research Assistant with the Uninhabited Aerial Vehicle Synthetic Aperture Radar group at NASA's Jet Propulsion Laboratory. From 1996 to 2004, he served on active duty in the U.S. Marine Corps. During that time, he was assigned to the Presidential Helicopter Squadron HMX-1, Marine Heavy Helicopter Squadron HMH-461, and HMM-264 as part of the 26th Marine Expeditionary Unit. As an undergraduate, he researched high-energy electromagnetic launchers at the Institute for Advanced Technology.

Cathleen E. Jones received the B.S. degree in physics from Texas A&M, College Station and the Ph.D. degree in physics from the California Institute of Technology, Pasadena, where she specialized in medium-energy experimental nuclear physics.

In 2004, she joined the Staff of the Radar Science and Engineering Section at the Jet Propulsion Laboratory, California Institute of Technology, where she worked on the development of the uninhabited aerial vehicle synthetic aperture radar (UAVSAR). She is Principal Investigator for the UAVSAR Gulf Oil Spill Campaign and is studying the effects of the oil in open water and coastal ecosystems. Her other work involves using DifInSAR techniques to monitor critical infrastructure, including a project studying levee stability and island subsidence in the Sacramento-San Joaquin Delta, and development of advanced algorithms for motion compensation in interferometric processing of data from airborne SAR instruments.

Benjamin Holt received the B.S. degree from Stanford University, Stanford, CA, in 1972 and the M.S. degree in physical oceanography from the University of Southern California, Los Angeles, in 1988.

He is a Research Scientist in the Oceans—Ice group within the Climate, Ocean, and Solid Earth Science Section at the Jet Propulsion Laboratory, California Institute of Technology, Pasadena, which he joined in 1978. His research interests involve the use of microwave remote sensing for sea ice and coastal oceanography.